Building and Environment 302 (2026) 114857

Contents lists available at ScienceDirect

Building and Environment

journal homepage: www.elsevier.com/locate/buildenv

A prognostic HVAC model for multi-physics urban simulations

Mojtaba Safdari[a], M. Nauman Ashraf[a], Mohammad Al Janaideh[a], Kamran Siddiqui[b], Amir A. Aliabadi[a,*]

[a] Department of Mechanical Engineering, College of Engineering, University of Guelph, Guelph, Ontario, Canada
[b] Department of Mechanical and Materials Engineering, Western University, London, Ontario, Canada

HIGHLIGHTS

- A prognostic HVAC model was developed for multi-physics urban simulations.
- The model enables two-way coupling of HVAC and outdoor microclimate systems.
- The model was validated for indoor/outdoor physical variables and energy consumption observations.
- VCWG v3.1.0 achieved $RMSE$ of ≈ 0.7°C and ≈ 7% for indoor temperature and relative humidity.
- A targeted benchmark and sensitivity analysis evaluated model advancements and key parameter effects.

ARTICLE INFO

Keywords:
Indoor-outdoor coupling
Model validation
Prognostic HVAC modeling
Thermal comfort
Urban building energy modeling
Urban microclimate modeling

ABSTRACT

This paper presents the development and experimental validation of the Vertical City Weather Generator (VCWG) v3.1.0, a unified single-solver framework that couples a prognostic urban canyon model with a dynamically resolved indoor heat and moisture balance model. The model is validated against high temporal resolution, co-located indoor–outdoor field measurements from an instrumented building in Guelph, Canada, over a July–April observation period spanning both cooling and heating seasons, with the simulation forced by on-site measured outdoor conditions (air temperature, relative humidity, wind, radiation, and precipitation). The prognostic formulation demonstrates high fidelity, reproducing the hourly indoor air temperature and relative humidity with Root Mean Square Error ($RMSE$) of ≈ 0.7°C and ≈ 7%, respectively. The model predictions of daily electricity and natural gas consumption are also in good agreement with observations, featuring $RMSE$ of ≈ 8.3 kWh and ≈ 3.4 m^3, respectively. Temporal tracking is strongest during periods with active cooling and heating demand, with Pearson's correlation coefficients of ≈ $r = 0.46$ for cooling-dominated electricity use and ≈ $r = 0.96$ for heating-dominated natural gas use. A targeted monthly benchmark against VCWG v3.0.0 and EnergyPlus, together with a one-factor-at-a-time sensitivity analysis, further evaluates model advancements and the influence of key parameters such as infiltration rate, internal heat gains, and HVAC control setpoints. These results show that VCWG v3.1.0 provides a practical multi-physics modeling platform for coupled urban canopy and building energy simulations, offering a field-evaluated tool for analyzing indoor–outdoor feedback, transient moisture/heat transport, and resilient urban technologies.

1. Introduction

Accurate representation of the interaction between buildings and their immediate surrounding microclimate has become an important direction in urban climate and energy modeling [1]. Buildings both respond to and actively modify local air temperature, radiation exchange, wind flow, and moisture conditions through heat/moisture exchange, surface storage of heat/moisture, shading, and other effects. These interactions occur on sub-hourly time scales that align with HVAC operation, moisture buffering, and occupant comfort response, making static or averaged boundary conditions fundamentally inadequate for urban physics simulations [2]. A growing body of work has shown that urban canyon

* Corresponding author.
Email addresses: msafdari@uoguelph.ca (M. Safdari), mashra03@uoguelph.ca (M.N. Ashraf), maljanai@uoguelph.ca (M. Al Janaideh), ksiddiq@uwo.ca (K. Siddiqui), aaliabad@uoguelph.ca (A.A. Aliabadi).
URL: www.aaa-scientists.com (A.A. Aliabadi).

https://doi.org/10.1016/j.buildenv.2026.114857
Received 11 March 2026; Received in revised form 20 May 2026; Accepted 8 June 2026
Available online 9 June 2026

microclimates can diverge substantially from standard meteorological conditions in rural areas, leading to systematic phase and magnitude errors in predicted indoor temperature, peak loads, and humidity when buildings are modeled as passive recipients of weather forcing [3,4]. For instance, a 2023 review by Sezer et al. notes that coupling urban microclimate models with building energy simulations yields more realistic results "that cannot be obtained in solo simulations" [5]. These findings highlight that without explicit coupling between building indoor environment and the surrounding microclimate, predictions of energy use and thermal comfort may fail to account for real urban climatic conditions, particularly in dense cities [6].

Parallel research has focused on outdoor thermal comfort, street-level microclimate, and the urban heat island, largely treating buildings as boundary conditions rather than dynamic participants [7–9]. Tools such as ENVI-met [10], CitySim Pro, and Orbital Stack [11] have been applied to quantify radiative exposure, pedestrian comfort, surface cooling strategies, vegetation performance, and the effects of local geometry [12]. These models excel at detailed outdoor physics, resolving wind flow, radiation exchange, and surface energy balances at fine spatial resolutions [11]. Their weakness lies indoors: they rely on simplified or fixed indoor conditions without physically based HVAC behavior, humidity control, or comfort modeling [13–15].

A separate line of work addresses the building interior using detailed energy simulation environments such as EnergyPlus [16], Carrier's Hourly Analysis Program (HAP) [17], TRNSYS [18,19], and IES Virtual Environment (IESVE) [20,21]. These tools offer rich envelope models and extensive HVAC component libraries, making them well-suited for equipment sizing, control design, and indoor comfort analyses [22]. However, most of them depend on static weather files that cannot reflect microclimate variations created by surrounding structures, surface moisture, or evolving canyon dynamics [23,24]. A recent review by Worthy et al. emphasizes that reliance on these non-urban-specific, aggregated climate datasets creates a significant "simulation-to-reality gap" because they fail to characterize the high spatial and temporal granularity of urban microclimates or capture extreme weather events [1]. As a result, outdoor–indoor feedback is imposed unidirectionally through prescribed weather forcing rather than emerging dynamically from the urban context. Without a prognostic outdoor model, they remain unable to capture two-way interactions between the indoor environment and the outdoor urban climate [3,25].

The Vertical City Weather Generator (VCWG) was conceived to bridge this gap by coupling a reduced-order urban canyon model with a building energy module. VCWG v3.0.0 introduced an environmentally aware temperature and humidity setpoint controller, but it was built upon a simplified, first-order indoor model inherited from the original Urban Weather Generator (UWG) paradigm [26] (a paradigm shared by all prior versions, including VCWG v1.3.2, v1.4.4, v1.4.5, v1.4.9, v1.5.0, v1.6.1, v2.0.0, and v3.0.0) [27–34]. Prior models treated temperature and humidity as algebraic outcomes of a static load balance rather than as prognostic state variables with explicit thermal and moisture capacities. These models lacked the capacity to capture the physics of HVAC supply air mixing, coil processes, and thermal comfort estimation. Consequently, while aware of outdoor conditions, they could not dynamically simulate the indoor thermal-moisture response to short-term microclimate variability or transient HVAC operation [27].

In parallel, several mesoscale meteorological frameworks incorporate Urban Canopy Models (UCMs) with embedded building energy parameterizations, such as the Weather Research and Forecasting (WRF) model coupled with Building Energy Parameterization (BEP-BEM) [2,35] and the Town Energy Balance (TEB) scheme [36–38]. These approaches capture two-way interactions between buildings and the atmospheric boundary layer and are well suited for city-scale urban heat island analyses. However, their internal building representations are primarily parameterized for large-scale climate feedbacks rather than resolving zone-level thermodynamic states [39]. In particular, indoor temperature and humidity are not modeled as explicit prognostic variables with detailed air-side HVAC sensible and latent processes or full indoor psychrometric evolution. As a result, they are not designed for neighborhood-scale studies requiring detailed indoor thermal and moisture comfort dynamics [1,40].

VCWG v3.1.0 addresses key limitations of existing building and urban microclimate modeling frameworks by moving from a static indoor load formulation to a prognostic indoor–outdoor system. Earlier VCWG versions, including v2.0.0 [28] and v3.0.0 [32], refined canyon-scale radiation and surface processes but retained a simplified, static indoor representation. In v3.1.0, indoor thermal and moisture states evolve dynamically in response to the simulated urban canyon microclimate, and the resulting sensible and latent heat rejection feeds back to the canyon within a native two-way coupling. Indoors, the framework employs a reduced-order air-side HVAC model that resolves mixed air conditions, explicit sensible and latent processes, indoor specific humidity evolution, and comfort indices, while distinguishing coil duty used for equipment energy accounting from the sensible and latent fluxes delivered to the indoor air state. Outdoors, the canyon formulation retains radiation trapping, vertical thermal structure, anthropogenic heat, and surface–atmosphere moisture exchange through an urban hydrology module. The intent is a physically transparent internally coupled framework that reduces the synchronization and data-exchange burden associated with external co-simulation interfaces [5,41] while remaining computationally practical for long-duration neighborhood-scale studies.

Table 1 summarizes core architectural capabilities across representative building energy simulators and urban microclimate models. The symbols reflect native functionality in standard workflows and do not account for custom couplings or external co-simulation interfaces. The

Table 1
Capability matrix comparing VCWG v3.1.0 with representative building-scale simulators and urban microclimate tools.

Aspect	VCWG v3.1.0	Energy Plus	IESVE	HAP	ENVI-met	CitySim Pro	TRNSYS
Detailed HVAC components and plant loops	△	✓	✓	△	✗	△	✓
Reduced-order air-side HVAC with explicit sensible and latent exchange	✓	△	△	△	✗	△	△
Prognostic indoor temperature and specific humidity state variables	✓	✓	✓	△	✗	△	△
Indoor comfort indices (PMV, PPD, adaptive comfort)	✓	✓	✓	✗	✗	✗	△
Prognostic urban canyon microclimate with vertical profiles	✓	✗	✗	✗	△	✗	✗
Outdoor hydrology and soil moisture feedback	✓	△[a]	✗	✗	✓	✗	✗
Native two-way indoor–canyon heat and moisture feedback	✓	✗	✗	✗	△	✗	△[b]
Integrated indoor–outdoor simulation without external co-simulation	✓	✗	✗	✗	✗	△	△[b]

✓ Full support, △ Partial or limited support, ✗ Not supported in the core workflow. *Note:* Symbols summarize native capabilities in the standard workflow. Many tools can extend scope through third party couplings, custom scripting, or specialized modules, which are not accounted for here unless they are commonly used as part of the core distribution.

[a] EnergyPlus includes detailed heat and moisture transfer in envelopes and specialized options such as green roof type models, but it does not provide a city scale urban hydrology engine comparable to an urban canopy scheme.

[b] TRNSYS can participate in coupled workflows via data exchange or co-simulation, but this depends on the external microclimate model and a user-implemented interface rather than a built-in urban microclimate module.

matrix is intended to clarify differences in modeling philosophy rather than to rank tools by accuracy. Because this conceptual comparison does not by itself quantify model performance, the Results and Discussion Section 3 also includes a targeted monthly energy benchmark against both VCWG v3.0.0 and EnergyPlus v26-1-0 for the same building and validation period. This comparison evaluates the advancement of VCWG v3.1.0 relative to a previous VCWG version while also providing an external reference against a widely used detailed building energy simulator.

The comparison highlights a structural divide in the literature. Detailed building engines such as EnergyPlus, IESVE, TRNSYS, and HAP provide rich HVAC component and envelope modeling but rely on prescribed weather inputs and do not resolve a prognostic urban canyon environment. Microscale outdoor models such as ENVI-met resolve canyon radiation, surface energy exchange, and atmospheric dynamics, yet they do not include a native, humidity-resolving indoor air model with active HVAC feedback. Co-simulation approaches can bridge these domains, but they require external data exchange between independent solvers. While external coupling avoids the need to build new models from scratch and preserves the strengths of specialized tools, it can introduce incompatible time scales between building and urban climate solvers, intermediate data-exchange requirements, and increased computational demand [5].

Within this landscape, VCWG v3.1.0 occupies a distinct modeling regime. It integrates a prognostic urban canyon formulation, a reduced-order air-side HVAC model with explicit sensible and latent processes, and dynamic indoor temperature and humidity states within a single computational framework. Heat and moisture rejected by the building feed back directly to the canyon, enabling two-way interaction without external coupling. This configuration supports physically consistent neighborhood-scale simulations while maintaining computational tractability. Pan et al. note that the building energy modeling field is currently undergoing a revolution, expanding toward urban-scale modeling and digital twins. However, they warn that striking a practical balance between the computational speed required for these massive scales and the accuracy needed for dynamic operational optimization remains a major challenge [42]. By integrating dynamic indoor temperature and humidity states within a single computational framework, VCWG v3.1.0 provides a practical balance of physical transparency and computational efficiency for these advanced applications.

The single-solver implementation in VCWG v3.1.0 is not intended to imply universal accuracy superiority over external VCWG–EnergyPlus co-simulation. The two approaches serve different modeling needs: external co-simulation is better suited for detailed multi-zone buildings, complex HVAC systems, and tall-building cases requiring height-resolved microclimate and HVAC heat-rejection exchange [3]. By contrast, VCWG v3.1.0 provides an internally coupled framework for long-duration building energy, comfort, humidity, and urban microclimate simulations by synchronizing the canyon model, radiation model, indoor heat and moisture balances, HVAC response, and comfort-control logic within one computational framework. This reduces external data-exchange and solver-synchronization burdens [5], while providing a computationally efficient alternative for long-duration studies focused on comfort control, humidity dynamics, HVAC loads, and urban microclimate feedback.

The computational value of this architecture is also relevant for high-repetition simulation workflows. Previous VCWG applications [30,34] have used the single-solver structure in evolutionary optimization studies requiring up to multiple thousands of model evaluations per case. In such settings, avoiding external message passing, repeated file exchanges, and solver synchronization between independent programs becomes important for computational feasibility.

This paper presents two main contributions. The first is the development of a physically based indoor air model that replaces static load formulations with a prognostic heat and moisture balance, in which indoor temperature and specific humidity evolve as state variables with explicit sensible and latent HVAC processes. Within this framework, indoor thermal and moisture conditions respond dynamically to simulated canyon microclimate variability. The formulation is implemented within a single computational framework in which building heat and moisture fluxes feed back directly to the prognostic canyon model. This architecture enables native two-way indoor–outdoor coupling while reducing the synchronization, data-exchange, and timescale-management challenges associated with external co-simulation. This paper positions this architecture as a computationally efficient internally coupled framework for long-duration comfort, humidity, HVAC, and urban microclimate studies, rather than as a universal replacement for high-fidelity external co-simulation workflows.

The second contribution is the validation and evaluation of this formulation using long-term, co-located indoor–outdoor field measurements collected under real operating conditions. The results demonstrate that the reduced-order air-side HVAC representation reproduces observed indoor temperature, humidity, energy consumption, and comfort dynamics with acceptable agreement while remaining computationally tractable for long-duration neighborhood-scale applications. The evaluation is further supported by a targeted monthly benchmark against VCWG v3.0.0 and EnergyPlus v26-1-0, and by a one-factor-at-a-time sensitivity analysis of infiltration rate, internal heat gains, and HVAC control setpoints.

2. Methodology

2.1. Model architecture and comparative positioning

Table 2 summarizes the stepwise development of the UWG framework toward VCWG v3.1.0 by highlighting the key physical, control, and system-level extensions introduced at each milestone. The original UWG formulation emphasized a compact urban canopy energy balance coupled to a simplified, load-based indoor representation with fixed

Table 2
Milestone progression toward VCWG v3.1.0. Symbol columns provide a visual summary of when key capabilities become core features, while the final column states the dominant extension at each stage.

Version	Urban Physics	Hydrology	Control	Indoor HVAC	Humidity & Latent	Dominant Extension
UWG (Original)	△	✗	✗	✗	✗	Compact canopy energy balance with load-based indoor representation and fixed operation.
VCWG v1.4.5	✓	✗	✗	✗	△	Vertical diffusion formulation in the canyon with expanded system-level alternative energy options and early rule-based operation.
VCWG v2.0.0	✓	✓	✗	✗	△	Explicit surface water storage and evaporation via a hydrology scheme, strengthening moisture pathways in canyon exchange.
VCWG v3.0.0	✓	✓	✓	✗	△	Environmentally aware operation through fuzzy-logic control that responds to indoor and outdoor conditions, with limited humidity handling.
VCWG v3.1.0	✓	✓	✓	✓	✓	Prognostic indoor humidity and latent balance added on top of v3.0.0 control, via explicit air-side HVAC and psychrometric processes, enabling comfort-driven closed-loop indoor–outdoor coupling.

✓ Full support, △ Partial or limited support, ✗ Not supported in the core workflow.

operation. VCWG v1.4.5 introduced the vertical diffusion formulation in the canyon and broadened the framework to support alternative energy systems, while keeping the indoor model load-based. VCWG v2.0.0 strengthened the outdoor physics by adding a surface hydrology scheme that explicitly represents surface water storage, evaporation, and moisture exchange within the canyon. VCWG v3.0.0 shifted the focus toward intelligent operation through an environmentally aware controller based on fuzzy logic, enabling HVAC response to adapt to indoor and outdoor conditions, albeit with limited humidity handling. VCWG v3.1.0 completes the transition to a prognostic indoor-outdoor system by introducing explicit air-side HVAC calculations and prognostic moisture and temperature evolution, along with dynamic heat and moisture storage and a comfort-driven smart controller. This progression reflects a deliberate evolution from geometry-focused canopy modeling toward an integrated, physics-based, and control-aware indoor-outdoor simulation framework.

Fig. 1 presents the integrated structure of VCWG. The framework couples a rural reference column, based on Monin-Obukhov Similarity Theory (MOST) [43], with an urban canyon column that resolves vertical turbulent diffusion and surface exchanges. Both rural and urban domains include radiation models and surface and soil energy-water balance components, ensuring consistent conservation of heat and moisture across the land-atmosphere system. The urban module further incorporates a building energy model that dynamically interacts with canyon air conditions. In the present formulation, the building energy model includes a fully prognostic HVAC representation, where sensible and latent fluxes are delivered through capacity-limited air-side processes and evolve consistently with the transient indoor energy and moisture balances.

Fig. 2 presents a conceptual schematic of the physical structure implemented in VCWG v3.1.0. The schematic illustrates the two-way coupling between the urban canyon microclimate, the indoor air node, and the HVAC system, driven by measured outdoor forcing variables. Outdoor boundary conditions, including air temperature, relative humidity, wind, radiation, precipitation, and soil state, are imposed on the urban canyon model, which resolves radiation trapping, surface energy and water balance, anthropogenic heat release, and hydrological processes. The canyon model exchanges sensible and latent heat with the indoor air node, where indoor air temperature, specific humidity, mean radiant temperature (MRT), and thermal comfort evolve prognostically. The HVAC system interacts directly with the indoor air node through mixed-air conditions and sensible and latent conditioning processes, while rejecting waste heat and moisture back to the urban canyon.

2.2. Experimental data collection and processing

To evaluate the accuracy of the new HVAC model within VCWG, the model is tested against measurements collected from a fully instrumented building in Guelph, Ontario. The building is used by real occupants as an office. Fig. 3 summarizes the workflow. Outdoor forcing variables and indoor sensor measurements are first processed and quality-checked. VCWG then simulates indoor temperature, humidity, and HVAC behavior using the prognostic formulation. Finally, simulated and measured time series are compared using standard performance metrics.

The validation dataset comes from long-term and co-located monitoring of the building and its immediate outdoor environment, summarized in Table 3 and illustrated in Fig. 4, which provides the sensor layout schematic with numbered labels matching the table. Indoors, an occupant-level sensor assembly (Items 1 to 5) resolves conditions at 1–1.6 m from the floor, including air temperature and relative humidity, MRT, and air speed, and also measures interior wall, ceiling, and floor surface temperatures using a thermocouple array to constrain interior surface temperature behavior [44]. The indoor sensor assembly was installed near an interior partition wall rather than an exterior corner and was not placed directly in a ventilation channel or supply air path. This location was selected to provide a stable long-term monitoring point in an occupied office space while reducing disturbance to the instruments. Whole-building electricity and natural gas consumption were recorded daily. The outdoor on-site weather station and supplementary sensors (Items 1 to 10) measured air temperature (2 m above the ground), air humidity (at 2 m), wind speed (2 m and 10 m), net radiation (2 m),

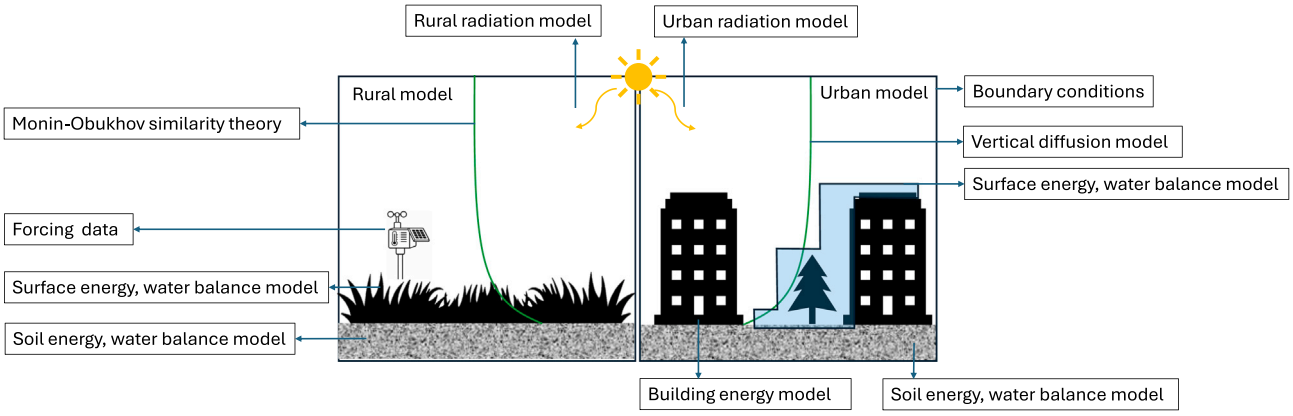

Fig. 1. Overall architecture of VCWG v3.1.0 showing the coupling between rural and urban columns, radiation models, surface and soil energy-water balance modules, vertical diffusion, and the building energy model with prognostic HVAC control and two-way coupling.

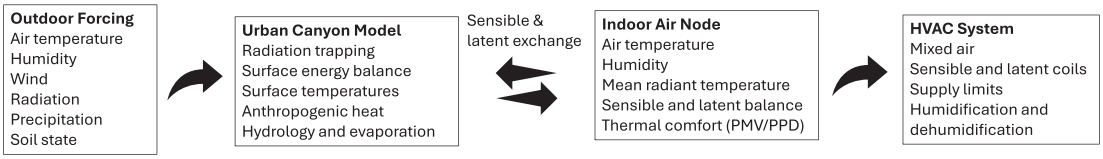

Fig. 2. Conceptual schematic of VCWG v3.1.0 illustrating two-way coupling between outdoor forcing variables, the urban canyon model, the indoor air node, and the HVAC system.

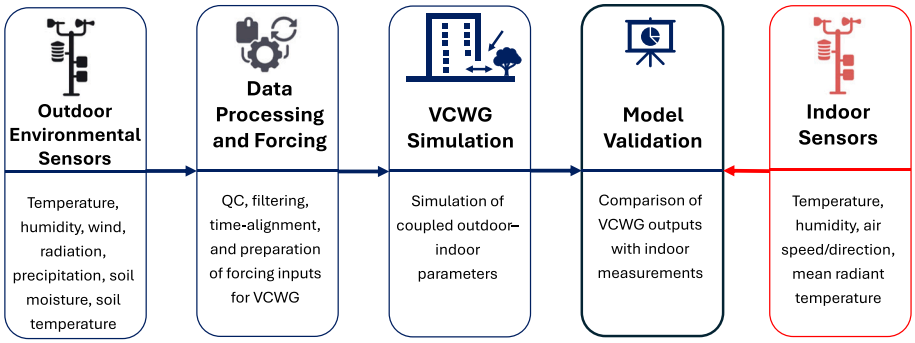

Fig. 3. Workflow used in this study, showing data acquisition, VCWG simulation, and model evaluation.

Table 3
Summary of sensors for environmental monitoring used in this study.

Variable: Sensor	Sampling	Range	Accuracy	Elevation
Wind: RM Young (81000) ultrasonic anemometer (1)	10 min	0–25 m s^{-1}	0.05 m s^{-1}	10 m
Wind: RM Young (81000) ultrasonic anemometer (2)	10 min	0–25 m s^{-1}	0.05 m s^{-1}	2 m
Air temperature, humidity: Vaisala (HMP155) (3)	10 min	−80–60 °C, 0–100%	0.2 °C, 2%	2 m
Precipitation: Young (52202) tipping bucket gage (4)	10 min	> 0.1 mm	3%	2 m
Radiation: Kipp & Zonen (CNR4) net radiometer (5)	10 min	305–2800 nm, 4.5-42 μm	5%, 10%	2 m
Soil temperature, moisture: Campbell Scientific (CS650) (6)	10 min	−50–70 °C, 0–100%	0.5 °C, 3%	−0.3 m
Precipitation: Lufft (WS100) radar (7)	1 min	> 0.01 mm	10%	10 m
Data logger: Campbell Scientific (CR6) (8)	–	–	–	–
Thermal images: FLIR (T530) (9)	4 hr	−20–120 °C	2 °C	1, 6 m
Data logger: Campbell Scientific (CR310) (10)	–	–	–	–
Mean radiant temperature: CS Black Globe (C108) (1)	1 min	−5-95 °C	0.3 °C	1 m
Wind: RM Young (81000) ultrasonic anemometer (2)	10 s	0–10 m s^{-1}	0.05 m s^{-1}	1.6 m
Data logger: Campbell Scientific (CR6) (3)	–	–	–	–
Air temperature, humidity: Vaisala (HMP155) (4)	1 min	−80–60 °C, 0–100%	0.2 °C, 2%	1 m
Surface temperature: Type E thermocouple (5)	1 min	0–50 °C	1 °C	0, 1.2, 3 m

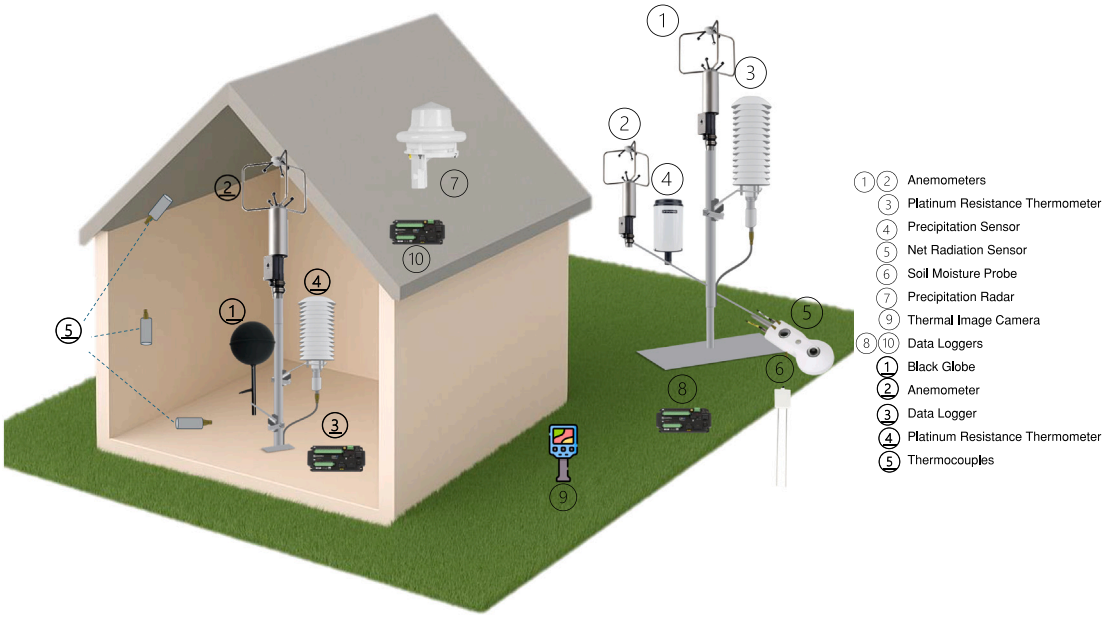

Fig. 4. Schematic sensor layout for the validation dataset. Outdoor sensors provide meteorological forcing (wind, air temperature and humidity, radiation, precipitation, and soil state), while indoor sensors provide occupant-level validation targets (air temperature, relative humidity, mean radiant temperature, air speed, and surface temperatures). Sensor IDs correspond to Table 3.

precipitation (2 m and 15 m), soil moisture (−0.3 m), and soil temperature (−0.3 m), and it also included a thermal camera used to map exterior wall and roof surface temperatures at scheduled intervals on selected days [45–47]. Precipitation was measured using both a tipping bucket gage (2 m) and a radar unit (15 m) to capture event timing and intensity at high temporal resolution. Multiple data loggers (Items 8, 10, 3) synchronized all measurement streams to a common time base prior to screening, gap handling, and model evaluation. These measurements

Table 4
Building parameters.

Parameter	Value
Climate zone	6A (Guelph, ON)
Floor area [m^2]	100
Building height [m]	3
Number of floors	1
Glazing ratio	0.4
Occupancy density [people m^{-2}]	0.03
Wall, roof, window R-values [m^2 K W^{-1}]	3.60, 5.46, 0.33
Infiltration air change rate [h^{-1}]	2
Supply air flow rate [m^3 m^{-2} s^{-1}]	0.01
Fresh air rate [L m^{-2} s^{-1}]	0.5
Internal gains [W m^{-2}]	6
Supply air temperature limits [°C]	50 (heating), 13 (cooling)
Rated cooling COP [-]	4.0
Heating efficiency [-]	0.70

prescribe the VCWG boundary conditions and provide independent targets for evaluating predicted indoor states, the prognostic indoor temperature and moisture evolution, and derived comfort metrics under realistic operating conditions. Although this deployment provides continuous co-located indoor and outdoor measurements, future validation studies would benefit from multiple indoor sensor locations to quantify within-zone spatial variability in temperature and humidity.

Data processing focused on producing temporally consistent forcing and validation series. Screening removed physically inconsistent readings, corrected obvious spikes, and aligned timestamps across all channels. Short gaps were handled through interpolation when appropriate, and the resulting outdoor time series were aggregated to the VCWG forcing time step, while indoor records were retained at their native resolution and resampled only as needed to support one-to-one comparisons during evaluation.

Key building properties required by VCWG, such as floor area, number of floors, envelope R-values, infiltration rate, ventilation assumptions, internal gains, and HVAC configuration, were compiled from construction documents and equipment records. Table 4 summarizes the values used.

Two additional evaluation steps were added to support the model exploration regarding parameter sensitivity and model benchmarking. First, a one-factor-at-a-time sensitivity analysis was conducted to evaluate how key uncertain building and control parameters influence monthly energy predictions. The analysis focused on the three parameter groups identified as most relevant to the validation: infiltration rate, internal heat gains, and HVAC control setpoints. January 2026 and August 2025 were selected as representative heating and cooling season months, respectively. For each sensitivity case, only one parameter was changed while all other parameters were kept fixed at their baseline values in Table 4. This design isolates the directional effect of each parameter and avoids confounding interactions among simultaneous parameter changes. The sensitivity outputs were evaluated using monthly electricity consumption and monthly natural gas consumption, which directly reflect cooling season and heating season HVAC responses.

Second, to provide both an internal model-family reference and an external building-energy reference, two additional simulations were prepared for the July 2025–April 2026 validation period. VCWG v3.0.0 was run using the same building and measured outdoor forcing assumptions where applicable to evaluate the improvement introduced by the new prognostic indoor heat and moisture formulation in VCWG v3.1.0. An EnergyPlus v26-1-0 model of the same building was also prepared using shared baseline properties where physically transferable, including weather forcing, location, run period, building geometry, glazing characteristics, envelope thermal properties, wall thermal resistance treatment, internal gains, ventilation and infiltration assumptions, operating schedules, HVAC control setpoints, humidity control setpoints, supply air temperature limits, HVAC efficiency assumptions, occupant heat split, radiant fractions, and service water heating assumptions. The purpose of this comparison was not to perform a full multi-platform calibration study, but to provide a practical monthly benchmark for electricity and natural gas consumption under comparable input assumptions. The results from VCWG v3.1.0, VCWG v3.0.0, and EnergyPlus v26-1-0 were compared with observations using monthly energy consumption relative to observations.

2.3. VCWG v3.1.0 prognostic HVAC model formulation

Earlier VCWG versions used a diagnostic approach, in which indoor temperature and specific humidity were solved assuming instantaneous thermal and humidity balance at each time step. This assumption neglects the building's thermal and humidity inertia, and, hence, the simulated indoor temperature and humidity dynamics, especially during the morning warm-up and evening cool-down periods, were not predicted accurately and realistically.

In the new prognostic formulation, indoor air temperature and humidity evolve according to coupled energy and moisture balance equations:

$$C_a \frac{\Delta T_{in}}{\Delta t} = \sum \dot{Q}_{sens}, \tag{1}$$

$$m_a \frac{\Delta q_{in}}{\Delta t} = \sum \dot{m}_w, \tag{2}$$

where the indoor air thermal capacity per unit building footprint area is defined as $C_a = \rho_{air}\, c_{air}\, H_{floor}\, N_{floors}$, with C_a [kJ m^{-2} K^{-1}] denoting the thermal capacity of indoor air per unit building footprint area, ρ_{air} [kg m^{-3}] the indoor air density, c_{air} [kJ kg^{-1} K^{-1}] the specific heat capacity of air, H_{floor} [m] the floor-to-ceiling height, and $N_{floors} = 1$ [-] the number of floors. The term $\dot{Q}_{sens}$ [kW m^{-2}] represents the net sensible heat flux to the indoor air node per unit building footprint area. The moisture balance is governed by the air mass capacity per unit footprint area, $m_a = \rho_{air}\, H_{floor}\, N_{floors}$, where m_a [kg m^{-2}] is the air mass per unit building footprint area, q_{in} [kg_v kg^{-1}] is the indoor specific humidity, and $\dot{m}_w$ [kg_v m^{-2} s^{-1}] denotes the net moisture flux from internal sources, ventilation, and infiltration. This formulation explicitly captures thermal and moisture storage in the indoor air volume, enabling realistic simulation of indoor temperature and humidity dynamics.

Figs. 5 and 6 provide a schematic overview of the coupled indoor energy and moisture formulation introduced in VCWG v3.1.0. The diagram summarizes the interaction between mixed-air conditions, thermostat logic, HVAC operation, and the prognostic evolution of indoor temperature and humidity within each simulation timestep. Sensible and latent processes are solved concurrently, with humidification (during heating) and dehumidification (during cooling) conditionally enabled based on the active HVAC mode. The schematic serves as a road map for the governing equations presented below.

HVAC control and capacity constraints. In VCWG v3.1.0, the HVAC system acts as a controlled source of sensible and latent energy that responds to indoor conditions through thermostat and humidistat logic. The system does not prescribe indoor temperature or humidity directly; instead, it delivers bounded sensible heat, $\dot{Q}_{HVAC}$ [kW m^{-2}], and moisture exchange, $\dot{m}_w$ [kg_v m^{-2} s^{-1}], that enter the prognostic energy and moisture balance equations.

Mixed-air conditions. The HVAC system conditions a mixed air stream composed of outdoor and return air. The mixed-air temperature and specific humidity are computed as

$$T_{mix} = f_{OA} T_{out} + (1 - f_{OA}) T_{in}, \tag{3}$$

$$q_{mix} = f_{OA} q_{out} + (1 - f_{OA}) q_{in}, \tag{4}$$

where T_{mix} [K] and q_{mix} [kg_v kg^{-1}] are the temperature and specific humidity of the mixed air stream entering the HVAC coil, respectively. The

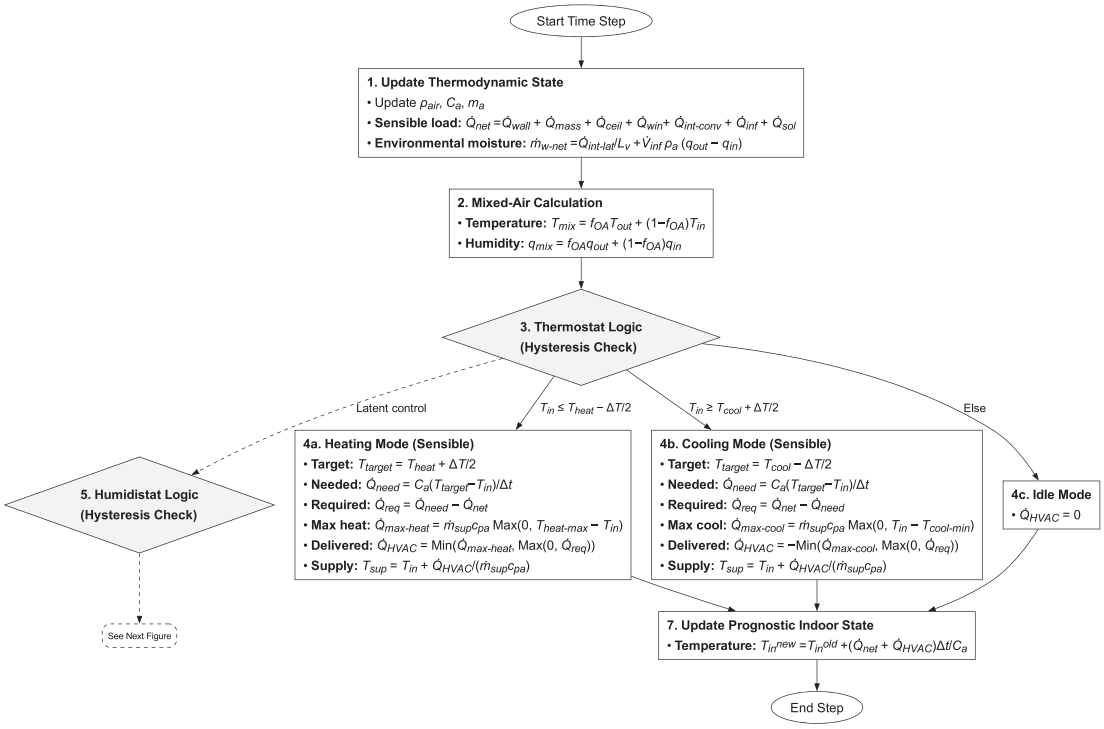

Fig. 5. Algorithm for the coupled indoor energy and moisture balance in VCWG v3.1.0. This framework illustrates the sequential evaluation of thermostat logic (sensible control) and humidistat logic (latent control), with the detailed sub-routines for latent processes detailed in Fig. 6.

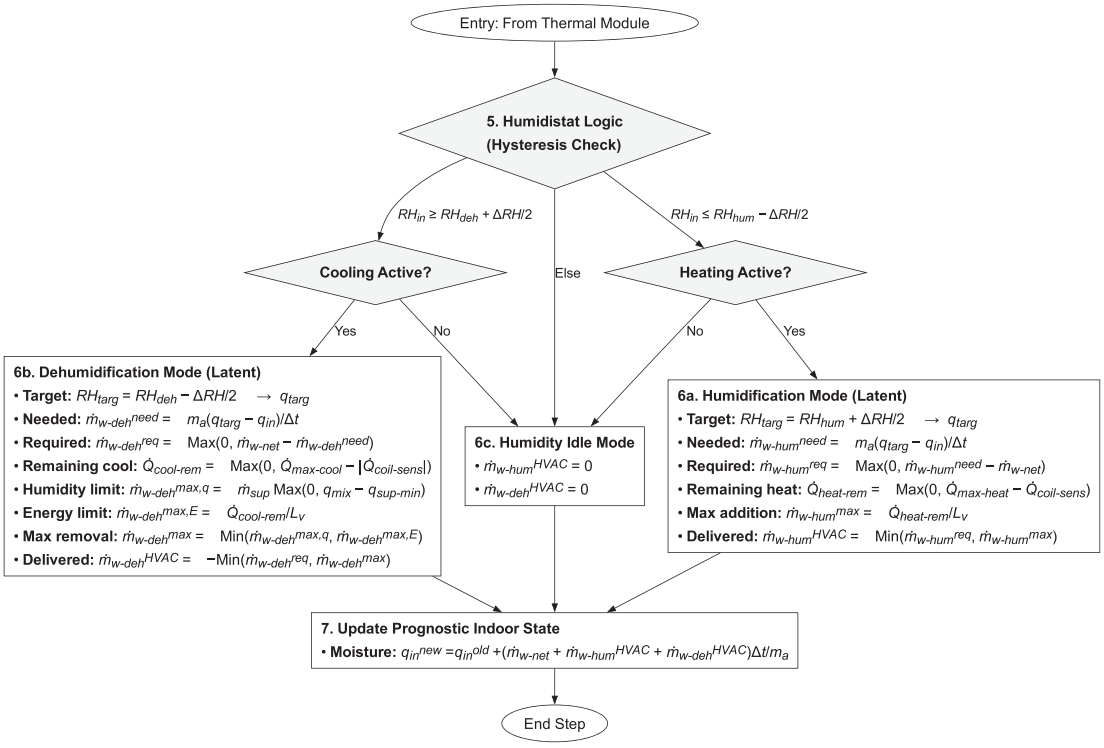

Fig. 6. Algorithm for indoor humidity regulation in VCWG v3.1.0. The diagram illustrates the humidistat-based control logic governing latent processes, including humidification and dehumidification modes, and the associated moisture balance used to update indoor specific humidity at each timestep.

variables T_{out} [K] and q_{out} [$kg_v\ kg^{-1}$] denote outdoor air temperature and specific humidity, and T_{in} [K] and q_{in} [$kg_v\ kg^{-1}$] denote indoor air temperature and specific humidity. The parameter f_{OA} [-] is the outdoor-air fraction imposed by ventilation requirements.

Thermostat and humidistat control. System operation is governed by a four-mode thermostat

$$\mathrm{MODE} \in \{\mathrm{OFF},\ \mathrm{HEAT},\ \mathrm{COOL},\ \mathrm{AUTO}\}, \tag{5}$$

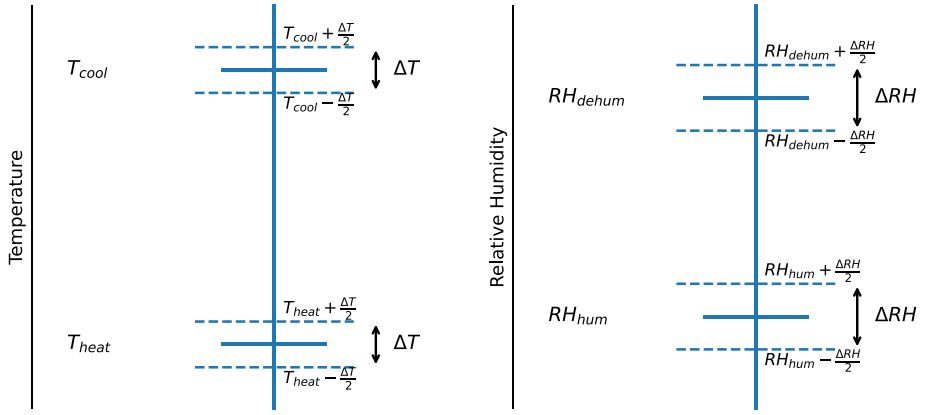

Fig. 7. Schematic representation of thermostat hysteresis control logic. The left panel illustrates temperature hysteresis bands around the heating and cooling setpoints, defined as $\pm\Delta T/2$. The right panel shows the analogous hysteresis structure for relative humidity control, defined as $\pm\Delta\mathrm{RH}/2$. Solid lines denote setpoints, while dashed lines indicate hysteresis bounds.

with hysteresis applied to both temperature and relative humidity setpoints to prevent rapid cycling. As illustrated in Fig. 7, each heating and cooling setpoint is surrounded by a symmetric hysteresis band of width ΔT, defined as $\pm\Delta T/2$ about T_{heat} and T_{cool}. The HVAC mode switches only when indoor conditions cross these bounds, ensuring stable operation across successive timesteps. At each timestep, the active mode determines whether sensible heating, sensible cooling, humidification, or dehumidification is permitted. Adaptive PMV and fuzzy control options available in VCWG were disabled in this study to isolate the physical response of the building HVAC system. A similar logic applies to relative humidity RH.

Sensible capacity constraints. For a given mode, the HVAC system attempts to meet the sensible load required to drive indoor temperature toward the target value within one timestep. The delivered or removed sensible heat in the HVAC system is calculated using the air mass flow rate, supply temperature, and mixed-air temperature. That is, $\dot{Q}_{\mathrm{coil}} = \dot{m}_{\mathrm{sup}} c_{\mathrm{pa}} (T_{\mathrm{sup}} - T_{\mathrm{mix}})$ [kW m^{-2}], where T_{sup} is constrained by equipment-specific minimum and maximum supply temperatures and $\dot{m}_{\mathrm{sup}}$ [kg m^{-2} s^{-1}] is the supply air mass flow rate. By applying the first law of thermodynamics to the HVAC system, the resulting effective supply air temperature is

$$T_{\mathrm{sup}} = T_{\mathrm{mix}} + \frac{\dot{Q}_{\mathrm{coil}}}{\dot{m}_{\mathrm{sup}} c_{\mathrm{pa}}}. \tag{6}$$

Latent capacity constraints. Latent control is evaluated concurrently with sensible control. During heating, humidification is limited by the available heating capacity required to evaporate water into the air stream. During cooling, dehumidification is limited by the cooling coil's ability to reduce the mixed-air humidity to its saturation value at the minimum cooling-coil temperature. The applied humidification and dehumidification rates therefore satisfy equipment-dependent upper bounds, and the net latent HVAC contribution enters the prognostic moisture balance.

Energy use. Once the delivered sensible and latent fluxes are determined, HVAC energy consumption is computed from the total coil duty. The sensible and latent coil components are aggregated as

$$\dot{Q}_{\mathrm{coil\text{-}tot}} = \dot{Q}_{\mathrm{coil\text{-}sens}} + \dot{Q}_{\mathrm{coil\text{-}lat}}, \tag{7}$$

where $\dot{Q}_{\mathrm{coil\text{-}sens}}$ and $\dot{Q}_{\mathrm{coil\text{-}lat}}$ [kW m^{-2}] are defined as non-negative magnitudes (active only in the corresponding operating mode). During cooling, the electricity use is computed as

$$\dot{W}_{\mathrm{cool}} = \frac{\dot{Q}_{\mathrm{coil\text{-}tot}}}{COP_{\mathrm{cool}}(t)}, \tag{8}$$

where the cooling COP is adjusted from the rated value using an outdoor-temperature modifier:

$$COP_{\mathrm{cool}}(t) = COP_{\mathrm{rated}} f_{\mathrm{COP}}(T_{\mathrm{out}}(t)). \tag{9}$$

The modifier is bounded to avoid unrealistic off-rated values:

$$f_{\mathrm{COP}}(T_{\mathrm{out}}) = \min\left[f_{\max}, \max\left(f_{\min}, 1 - s\left(T_{\mathrm{out}} - T_{\mathrm{rated}}\right)\right)\right]. \tag{10}$$

In this study, $COP_{\mathrm{rated}} = 4.0$, $T_{\mathrm{rated}} = 35°\mathrm{C}$, $s = 0.025\ °\mathrm{C}^{-1}$, $f_{\min} = 0.60$, and $f_{\max} = 1.20$ were used. During heating, the required fuel-side heat input is computed from the heating system efficiency as $\dot{Q}_{\mathrm{fuel}} = \dot{Q}_{\mathrm{coil\text{-}tot}}/\eta_{\mathrm{furnace}}$ [kW m^{-2}].

Figs. 8 and 9 define the control volumes and sign conventions used to derive the prognostic indoor updates in Eqs. (13) and (21). The algorithmic flowcharts in Figs. 5 and 6 describe the mode selection and sequencing, while the loop diagrams clarify how each physical exchange term enters the zone energy and moisture balances.

Fig. 8 shows the sensible heat balance on the indoor air node. Passive contributions from the envelope and zone processes, including convection from interior surfaces ($\dot{Q}_{\mathrm{wall}}$, $\dot{Q}_{\mathrm{mass}}$, $\dot{Q}_{\mathrm{ceil}}$), window heat transfer and solar gains ($\dot{Q}_{\mathrm{win}}$, $\dot{Q}_{\mathrm{sol}}$), internal convective gains ($\dot{Q}_{\mathrm{int\text{-}conv}}$), and infiltration ($\dot{Q}_{\mathrm{inf}}$), are grouped into the net zone load $\dot{Q}_{\mathrm{net}}$ in Eq. (11) all in [kW m^{-2}]. The HVAC sensible contribution $\dot{Q}_{\mathrm{HVAC}}$ [kW m^{-2}] enters the zone through the supply air stream, while the coil duty used for energy consumption is evaluated relative to the mixed-air state (T_{mix}) [K], consistent with Fig. 8.

The $\dot{Q}_{\mathrm{net}}$ [kW m^{-2}] sensible load component is

$$\dot{Q}_{\mathrm{net}} = \dot{Q}_{\mathrm{wall}} + \dot{Q}_{\mathrm{mass}} + \dot{Q}_{\mathrm{ceil}} + \dot{Q}_{\mathrm{win}} + \dot{Q}_{\mathrm{int\text{-}conv}} + \dot{Q}_{\mathrm{inf}} + \dot{Q}_{\mathrm{sol}}, \tag{11}$$

where $\dot{Q}_{\mathrm{net}}$ [kW m^{-2}] is the net sensible heat flux to the indoor air node per unit building footprint area. The individual terms are defined by standard heat balance expressions, i.e., $\dot{Q}_{\mathrm{wall}} = A_{\mathrm{wall}} h_w (T_{\mathrm{wall}} - T_{\mathrm{in}})$, $\dot{Q}_{\mathrm{mass}} = A_{\mathrm{mass}} h_m (T_{\mathrm{mass}} - T_{\mathrm{in}})$, $\dot{Q}_{\mathrm{ceil}} = A_{\mathrm{ceil}} h_c (T_{\mathrm{ceil}} - T_{\mathrm{in}})$, $\dot{Q}_{\mathrm{win}} = A_{\mathrm{win}} U_w (T_{\mathrm{out}} - T_{\mathrm{in}})$, $\dot{Q}_{\mathrm{inf}} = \dot{V}_{\mathrm{inf}} \rho_a c_{pa} (T_{\mathrm{out}} - T_{\mathrm{in}})$, and $\dot{Q}_{\mathrm{sol}} = SHGC\, A_{\mathrm{win}} S$. Here, A_{wall}, A_{mass}, A_{ceil}, and A_{win} [m^2 m^{-2}] are the corresponding interior surface areas normalized by the building footprint area, h_w, h_m, and h_c [kW m^{-2} K^{-1}] are the interior convective heat transfer coefficients

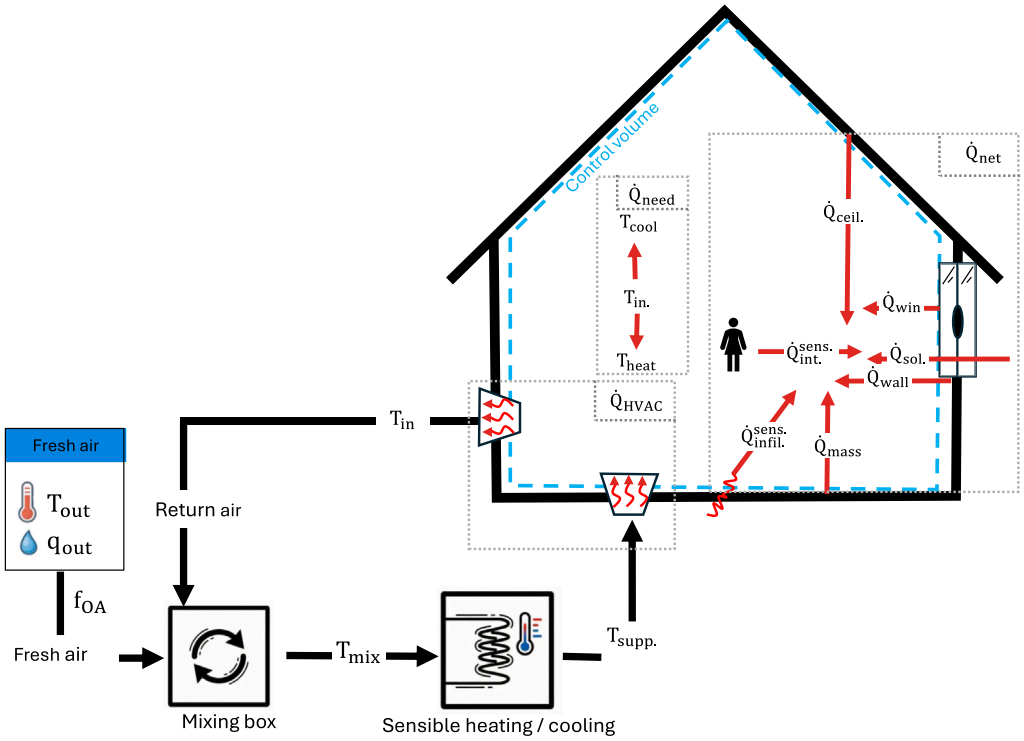

Fig. 8. Sensible heat balance control volume and HVAC loop configuration.

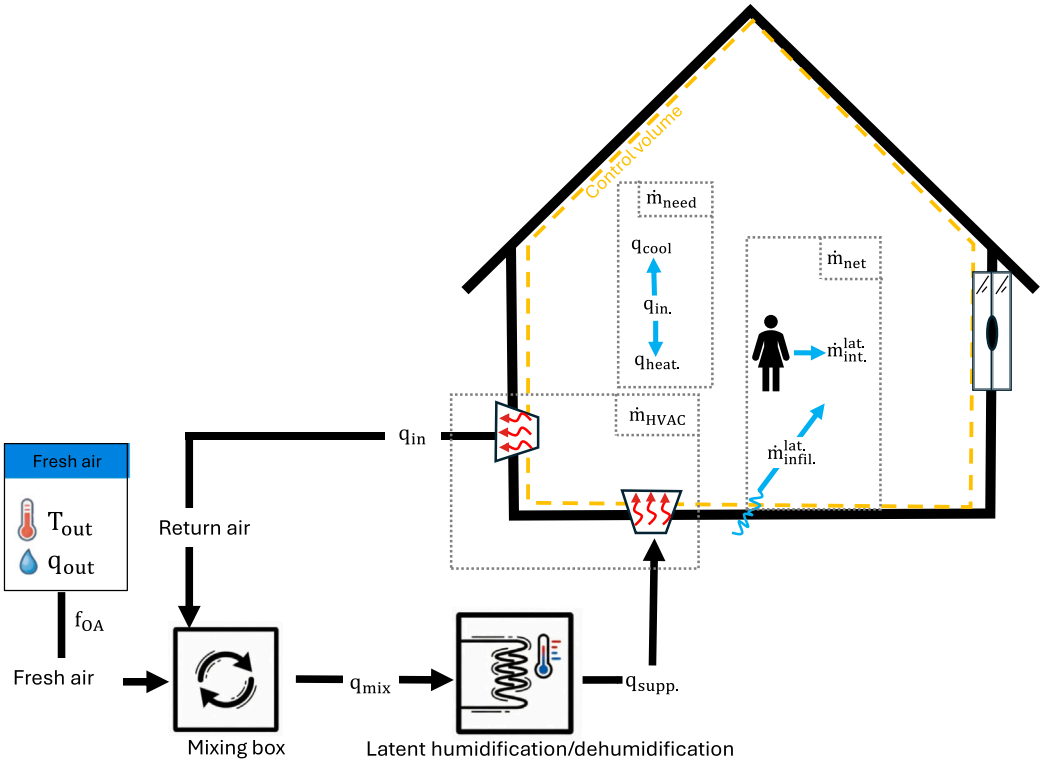

Fig. 9. Latent heat and moisture balance control volume and HVAC loop configuration.

for walls, internal mass, and ceiling, respectively, and U_w [kW m^{-2} K^{-1}] is the window overall heat transfer coefficient. The temperatures T_{wall}, T_{mass}, T_{ceil}, T_{out}, and T_{in} [K] denote the interior wall, internal mass, interior ceiling, outdoor air, and indoor air temperatures, respectively. The term $\dot{Q}_{int\text{-}conv}$ [kW m^{-2}] represents the convective fraction of internal sensible heat gains. The infiltration volumetric flow rate per unit footprint area is $\dot{V}_{inf}$ [m^3 m^{-2} s^{-1}], with ρ_a [kg m^{-3}] as the air density and c_{pa} [kJ kg^{-1} K^{-1}] as the air specific heat capacity. Solar heat gain through

windows is represented by Solar Heat Gain Coefficient ($SHGC$) [-], the incident solar irradiance on the window S [kW m^{-2}], and A_{win} [m^2 m^{-2}].

The term $\dot{Q}_{HVAC}$ is calculated according to Fig. 5 parts (a) to (c). Under heating mode (a), first a target temperature $T_{target} = T_{heat} + \Delta T/2$ is defined using the heating setpoint temperature T_{heat} and a hysteresis temperature ΔT (see Fig. 7). The heating rate required to reach the target boundary within one timestep is $\dot{Q}_{need} = C_a(T_{target} - T_{in})/\Delta t$. Accounting for the passive indoor sensible balance, the required HVAC contribution is $\dot{Q}_{req} = \dot{Q}_{need} - \dot{Q}_{net}$. The delivered heat is then $\dot{Q}_{HVAC} = \min(\dot{Q}_{max\text{-}heat}, \max(0, \dot{Q}_{req}))$. The maximum amount of deliverable heat is calculated using $\dot{Q}_{max\text{-}heat} = \dot{m}_{sup} c_{pa} \max(0,\ T_{heat\text{-}max} - T_{in})$, where $\dot{m}_{sup}$ is the supplied air mass flow rate [kg m^{-2} s^{-1}], and $T_{heat\text{-}max}$ is considered as the maximum deliverable temperature by the heating system. Under cooling mode (b), first a target temperature $T_{target} = T_{cool} - \Delta T/2$ is defined using the cooling setpoint temperature T_{cool} and a hysteresis temperature ΔT (see Fig. 7). The rate required to reach the target boundary within one timestep is $\dot{Q}_{need} = C_a(T_{target} - T_{in})/\Delta t$. Accounting for the passive indoor sensible balance, the required HVAC contribution is $\dot{Q}_{req} = \dot{Q}_{net} - \dot{Q}_{need}$. The delivered cooling is then implemented as $\dot{Q}_{HVAC} = -min(\dot{Q}_{max\text{-}cool}, \max(0, \dot{Q}_{req}))$. This maximum is derived using $\dot{Q}_{max\text{-}cool} = \dot{m}_{sup} c_{pa} \max(0,\ T_{in} - T_{cool\text{-}min})$, where $T_{cool\text{-}min}$ is the minimum feasible supply temperature delivered by the cooling system.

The corresponding effective supply air temperature under heating and cooling conditions can be computed by applying the first law of thermodynamics to the building air

$$T_{sup} = T_{in} + \frac{\dot{Q}_{HVAC}}{\dot{m}_{sup}\, c_{pa}}. \tag{12}$$

Under neither sensible heating nor cooling (c) $\dot{Q}_{HVAC} = 0$ kW m^{-2}. By applying the first law of thermodynamics and using an explicit time update, the indoor temperature evolves according to

$$T_{in}^{new} = T_{in}^{old} + \frac{(\dot{Q}_{net} + \dot{Q}_{HVAC})\Delta t}{C_a}. \tag{13}$$

The analogous moisture control volume is shown in Fig. 9. Environmental and internal moisture sources are represented by $\dot{m}_{w\text{-}net}$ in Eq. (14), combining infiltration-driven exchange with outdoor air and moisture generation associated with internal latent gains. The HVAC system then adds a bounded humidification or dehumidification term depending on the active mode, where humidification is limited by the remaining heating capacity after sensible heating has been accounted for, and dehumidification is limited by both the cooling coil's ability to reduce mixed-air humidity toward saturation at the minimum coil temperature and the remaining cooling capacity after sensible cooling has been accounted for. These terms enter the prognostic humidity update in Eq. (21), ensuring that latent control remains consistent with storage and air exchange in the zone.

The moisture balance follows a structure parallel to the sensible heat balance. The indoor specific humidity evolves from infiltration, internal latent sources, and the building's humidification and dehumidification equipment. Using the air mass of the zone as the control volume, the net moisture exchange to the zone driven by air exchange and internal latent sources is

$$\dot{m}_{w\text{-}net} = \dot{m}_{w\text{-}int} + \dot{m}_{w\text{-}inf} = \frac{\dot{Q}_{int\text{-}lat}}{L_v} + \dot{V}_{inf}\rho_a(q_{out} - q_{in}), \tag{14}$$

where $\dot{m}_{w\text{-}net}$ is the net moisture source to the zone air, $\dot{m}_{w\text{-}int}$ is moisture flux due to internal latent fluxes, and $\dot{m}_{w\text{-}inf}$ is moisture flux due to infiltration, all in [kg$_v$ m^{-2} s^{-1}]. L_v [kJ kg$_v^{-1}$] is latent heat of vaporization, $\dot{Q}_{int\text{-}lat}$ [kW m^{-2}] is internal latent heat, $\dot{V}_{inf}$ [m^3 m^{-2} s^{-1}] is infiltration flow, and q_{out}, q_{in} [kg$_v$ kg^{-1}] are the outdoor and indoor specific humidity.

The humidification system (a) activates when q_{in} falls below its lower hysteresis threshold ($RH_{hum} - \Delta RH\ /2$). To reach the upper switching threshold ($RH_{targ} = RH_{hum} + \Delta RH\ /2$) within one timestep Δt, and after converting the target relative humidity to specific humidity, the needed humidification rate is $\dot{m}_{w\text{-}hum}^{need} = m_a(q_{targ} - q_{in})/\Delta t$. Accounting for environmental moisture exchange, the required humidification rate becomes $\dot{m}_{w\text{-}hum}^{req} = \max(0,\ \dot{m}_{w\text{-}hum}^{need} - \dot{m}_{w\text{-}net})$.

Because moisture must be evaporated into the air stream, the maximum deliverable humidification is limited by the heating capacity that remains after sensible heating has been supplied during the same timestep. The remaining heating capacity is

$$\dot{Q}_{heat\text{-}rem} = \max\left(0,\ \dot{Q}_{max\text{-}heat} - \dot{Q}_{coil\text{-}sens}\right), \tag{15}$$

where $\dot{Q}_{coil\text{-}sens}$ [kW m^{-2}] is the sensible heating rate delivered during the same timestep. The maximum humidification rate is then

$$\dot{m}_{w\text{-}hum}^{max} = \frac{\dot{Q}_{heat\text{-}rem}}{L_v}. \tag{16}$$

This gives $\dot{m}_{w\text{-}hum}^{HVAC} = \min(\dot{m}_{w\text{-}hum}^{req}, \dot{m}_{w\text{-}hum}^{max})$.

Similarly, the dehumidifier system (b) activates when RH_{in} exceeds its upper hysteresis threshold ($RH_{deh} + \Delta RH\ /2$). The needed moisture removal to reach ($RH_{targ} = RH_{deh} - \Delta RH\ /2$) is $\dot{m}_{w\text{-}deh}^{need} = m_a(q_{targ} - q_{in})/\Delta t$. Accounting for environmental moisture exchange, the required dehumidification rate becomes $\dot{m}_{w\text{-}deh}^{req} = \max(0,\ \dot{m}_{w\text{-}net} - \dot{m}_{w\text{-}deh}^{need})$.

The maximum condensate removal is constrained by both a humidity-ratio limit and an energy-capacity limit. The humidity-ratio limit is

$$\dot{m}_{w\text{-}deh}^{max,q} = \dot{m}_{sup} \max(0,\ q_{mix} - q_{sup\text{-}min}), \tag{17}$$

where $\dot{m}_{sup}$ [kg m^{-2} s^{-1}] is supply air mass flow rate, q_{mix} [kg$_v$ kg^{-1}] is mixed-air specific humidity, and $q_{sup\text{-}min}$ [kg$_v$ kg^{-1}] is saturation specific humidity at the minimum cooling-coil temperature. To avoid using the same cooling capacity twice within the same timestep, the remaining cooling capacity after sensible cooling is

$$\dot{Q}_{cool\text{-}rem} = \max\left(0,\ \dot{Q}_{max\text{-}cool} - \left|\dot{Q}_{coil\text{-}sens}\right|\right), \tag{18}$$

where $\dot{Q}_{coil\text{-}sens}$ [kW m^{-2}] is the sensible cooling rate delivered during the same timestep. The corresponding energy-based dehumidification limit is

$$\dot{m}_{w\text{-}deh}^{max,E} = \frac{\dot{Q}_{cool\text{-}rem}}{L_v}. \tag{19}$$

The maximum dehumidification rate is then

$$\dot{m}_{w\text{-}deh}^{max} = \min\left(\dot{m}_{w\text{-}deh}^{max,q}, \dot{m}_{w\text{-}deh}^{max,E}\right). \tag{20}$$

Thus, the actual dehumidification rate becomes $\dot{m}_{w\text{-}deh}^{HVAC} = -\min\left(\dot{m}_{w\text{-}deh}^{req}, \dot{m}_{w\text{-}deh}^{max}\right)$.

Now using mass balance for moisture and using the same explicit update method, the indoor specific humidity evolves according to

$$q_{in}^{new} = q_{in}^{old} + \frac{\left(\dot{m}_{w\text{-}net} + \dot{m}_{w\text{-}hum}^{HVAC} + \dot{m}_{w\text{-}deh}^{HVAC}\right)\Delta t}{m_a}. \tag{21}$$

3. Results and Discussion

3.1. Monthly and daily model performance evaluation

Table 5 summarizes the monthly performance of the VCWG model against actual electricity and gas consumption (daily aggregates in the instrumented building) using three complementary metrics: Bias, Root Mean Square Error ($RMSE$), and Pearson's correlation coefficient (r). Bias is calculated as simulated minus observed consumption; therefore, negative Bias values indicate model underestimation, while positive Bias

Table 5
Monthly and pooled performance metrics comparing VCWG simulations with observed electricity and gas consumption from July 2025 to April 2026.

Period	Electricity			Gas		
	Bias [kWh]	$RMSE$ [kWh]	r	Bias [m^3]	$RMSE$ [m^3]	r
July	2.260	5.170	0.750	−0.072	0.411	−0.094
August	1.790	4.766	0.842	−0.105	0.387	0.676
September	−3.421	4.121	−0.119	−0.594	1.578	0.764
October	−5.720	6.333	0.094	−0.214	1.849	0.926
November	−7.127	7.462	N.C.	−1.288	2.960	0.703
December	−7.712	7.874	N.C.	−1.844	3.571	0.702
January	−9.937	13.444	N.C.	−0.960	5.772	0.594
February	−9.367	9.700	N.C.	−2.065	5.695	0.627
March	−9.257	9.779	0.116	−2.126	4.429	0.810
April	−9.048	9.427	−0.133	−1.775	3.341	0.846
All months pooled	**−5.711**	**8.261**	**0.464**	**−1.097**	**3.433**	**0.960**

N.C. denotes cases where Pearson's correlation coefficient was not calculated because the observed or simulated values had insufficient variability. Monthly Pearson's correlation values are reported where calculable, including weak or negative values, for transparency. These monthly values should be interpreted cautiously during low-variance periods.

values indicate overestimation. Bias and $RMSE$ quantify the direction and magnitude of model errors and remain interpretable across all operating regimes. Pearson's correlation coefficient is intended to assess agreement between simulated and observed *temporal patterns*, but it is only informative when the observed and simulated series exhibit sufficient variability. When the observed or simulated signal is nearly constant, the standard deviation approaches zero, making Pearson's r mathematically undefined or highly unstable. A primary example of this occurs during seasons when energy loads are governed almost entirely by baseline domestic usage. Because this usage remains relatively constant and lacks the significant shifts driven by heating or cooling demands, there is no meaningful variability for the correlation to capture. In these cases, r was not calculated and is reported as N.C. Where Pearson's r could be calculated, weak or negative values are reported for transparency, but month-specific correlations during low-variance periods are interpreted cautiously.

For monthly electricity consumption (Table 5), meaningful temporal variability occurs primarily during the cooling season. Accordingly, July 2025 and August 2025 show moderate to strong pattern agreement ($r = 0.750$ and 0.842). From September 2025 onward, electricity is increasingly dominated by occupant-driven base loads rather than weather-driven cooling, and the resulting low and irregular variability weakens the diagnostic value of monthly correlation. This is reflected in weak or negative monthly electricity correlations in September 2025 through April 2026, and in non-calculable values from November 2025 through February 2026. In parallel, the magnitude of the electricity error increases in the winter, with January 2026 exhibiting the largest underestimation (Bias = −9.937 kWh) and the largest $RMSE$ (13.444 kWh), consistent with baseline usage mismatches becoming more visible once cooling demand disappears. The negative Bias values from September 2025 through April 2026 indicate systematic underestimation of measured electricity use during the non-cooling and heating-season months.

Gas consumption behaves differently because it retains meaningful variability throughout the heating season. The model produces a fuel-side heating energy demand, which was converted to an equivalent natural gas volume to match the utility data. A higher heating value of 10.35 kWh m^{-3} was used [48,49]. Monthly gas correlations are positive from August 2025 through April 2026 ($r = 0.594$ to 0.926), indicating that VCWG captures the timing and temporal evolution of heating demand more consistently than electricity use. In July 2025, gas consumption is close to zero, and the correlation is weak and negative ($r = -0.094$), which is expected because the gas signal has limited variability during the non-heating period. As the heating season advances, errors increase, with the largest $RMSE$ occurring in January 2026 (5.772 m^3), followed closely by February 2026 (5.695 m^3). This suggests that day-to-day variability in heating operation is increasingly shaped by thermostat choices, ventilation practices, and schedules that are not fully prescribed in the model. Late-winter demand is also more sensitive to uncertainty in infiltration and ventilation, because wind and stack effects amplify air exchange when the indoor–outdoor temperature difference is the largest. In March 2026 and April 2026, gas $RMSE$ decreases to 4.429 and 3.341 m^3, respectively, while correlations remain strong ($r = 0.810$ and 0.846), indicating that the model continues to capture the heating-demand pattern during the late heating and shoulder-season period.

To address the limited interpretability of month-specific correlations under low-variance conditions, Pearson's correlation coefficient was also calculated using the pooled daily data across the full July 2025–April 2026 validation period. The pooled correlations are $r = 0.464$ for electricity and $r = 0.960$ for gas consumption. These results indicate moderate temporal agreement for electricity and strong temporal agreement for gas over the full monitoring duration. Therefore, the validation separates two aspects of performance: monthly Bias and $RMSE$ are used to evaluate magnitude agreement, while the pooled Pearson's correlation provides a more informative assessment of temporal tracking across the full validation period.

3.1.1. Daily energy consumption validation

Fig. 10 compares daily energy consumption from the building measurements with VCWG-simulated consumption under the same measured outdoor forcing. The figure is split into electricity (Fig. 10a) and natural gas (Fig. 10b), which together reflect the dominant seasonal end uses in the building, with electricity primarily associated with plug and equipment loads and summer cooling, and gas primarily associated with space heating during the cold season.

In Fig. 10(a), measurements began in July 2025, but only July 2025–September 2025 are shown because these months contain the periods where electricity consumption exhibits nontrivial variability and a visible seasonal transition. Outside this window, electricity consumption is largely dominated by baseline plug and equipment loads with weak weather-driven variability, so additional monthly panels would provide limited additional insight into model performance. For the months shown, the VCWG curve follows the observations closely in both magnitude and timing of changes, indicating that the model captures the dominant drivers of day-to-day electricity demand when forced by real outdoor conditions. July 2025 displays the largest variability and several short-term increases in electricity consumption. VCWG reproduces these fluctuations and the overall level, including the higher-demand periods

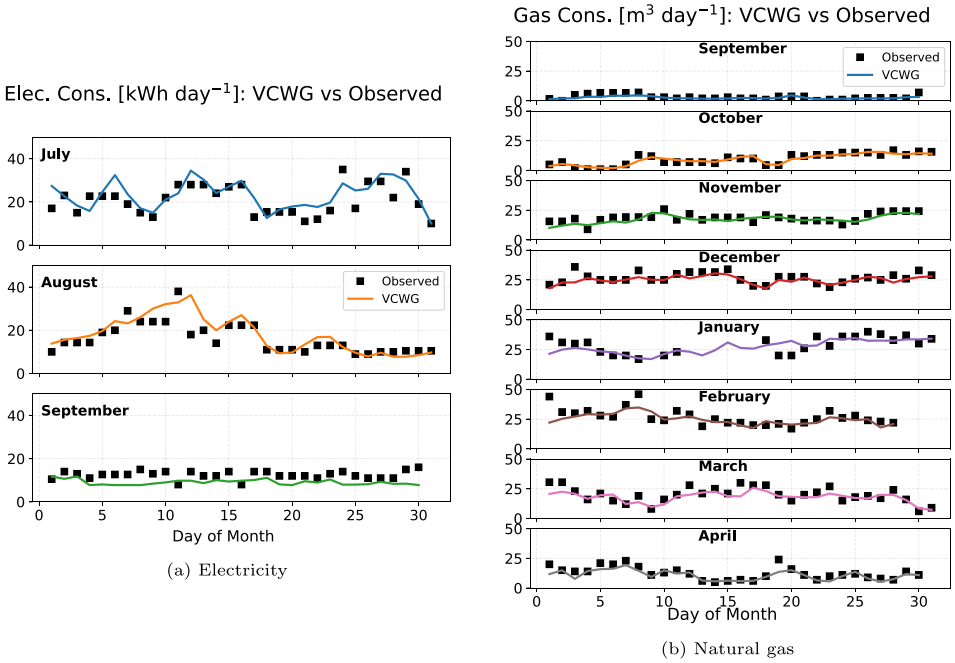

(a) Electricity

(b) Natural gas

Fig. 10. Daily observed and VCWG-simulated energy consumption for selected months under the conventional thermostat configuration. Markers indicate observations and solid lines indicate VCWG simulations. The natural gas panel covers September 2025 through April 2026 to represent the onset, progression, and late-season decline of heating demand.

and subsequent reductions. August 2025 shows a clearer structure with a rise toward mid-month followed by a pronounced drop and then lower electricity consumption later in the month; VCWG captures this evolution and the main turning points. September 2025 exhibits lower and more stable electricity demand compared to July 2025 and August 2025, consistent with reduced cooling requirements, and VCWG reproduces this shift and the reduced variability. Across all three months, the agreement suggests that the modeled cooling-related electricity response and its interaction with baseline electrical loads are represented realistically at the daily time resolution.

Fig. 10(b) presents gas consumption (including domestic hot water demand) for September 2025–April 2026, capturing the onset, progression, and late-season decline of the heating season. September 2025 shows gas use close to baseline, and VCWG remains near that level, reflecting minimal heating demand. In October 2025, observed gas consumption increases and becomes more variable as outdoor temperatures decline. VCWG captures both the gradual rise in demand and the main day-to-day variations. In November 2025, gas use increases further and the observations show sustained higher values with intermittent peaks; VCWG reproduces the elevated level and most of the short-term fluctuations. December 2025 marks sustained winter heating operation, with several multi-day periods of elevated demand that are closely followed by the model. January 2026 and February 2026 maintain high heating demand as outdoor temperatures remain low. The observations show persistently elevated gas consumption with moderate day-to-day variability, and VCWG reproduces the overall level and timing of these changes. March 2026 shows a transition from peak winter demand toward lower heating loads, while April 2026 reflects further decline as outdoor conditions become milder. VCWG captures this seasonal reduction and continues to reproduce the main temporal structure of heating demand under real weather forcing. Slightly larger deviations appear during some higher-demand periods in winter, but the model continues to capture the main temporal structure of heating demand under real weather forcing.

Fig. 11 summarizes model skill by comparing VCWG-simulated and observed daily energy consumption against the 1:1 perfect-agreement line. This view complements the monthly time series by showing magnitude agreement across the full range of loads and by revealing whether errors depend on season or demand level.

For electricity (Fig. 11a), the points for July 2025 and August 2025 span the widest consumption range and cluster around the 1:1 line, indicating that VCWG captures both moderate and high electricity-use days during cooling-dominated operation. Dispersion increases at higher consumption, which suggests larger errors on peak days, while the overall data cloud remains centered near the 1:1 line. September 2025 points occupy a narrower, low-consumption range and are tightly grouped, with a slight tendency to fall below the 1:1 line, indicating mild underestimation when electricity demand is relatively stable.

For natural gas (Fig. 11b), seasonal clustering is more pronounced as heating demand increases from September 2025 through April 2026. September 2025 points remain near the origin and close to the 1:1 line, consistent with near-baseline heating. October 2025 and November 2025 cover the mid-range and align closely with the 1:1 line, showing that VCWG reproduces the onset and strengthening of heating demand. December 2025, January 2026, and February 2026 span the highest gas-use days. Rather than showing a persistent bias, these peak winter months exhibit increased dispersion around the 1:1 line at the upper end. March 2026 occupies an intermediate range between the peak winter months and the lower shoulder-season loads, while April 2026 shifts toward lower gas consumption as heating demand declines. This indicates that while the model captures the overall magnitude of winter heating, the absolute day-to-day variance naturally grows at higher loads. This wider scatter in the winter cluster is consistent with the increased $RMSE$ reported in Table 5. Overall, the scatter plots confirm strong agreement across seasons, with the largest deviations presenting as bidirectional scatter during high-demand periods rather than as a systematic over- or under-prediction.

The electricity and gas panels show consistent agreement between observed and simulated daily consumption during periods of active energy use. The model reproduces both the seasonal shifts in dominant end uses and the day-to-day variability within each month. The gas comparison also captures the transition from peak winter heating demand

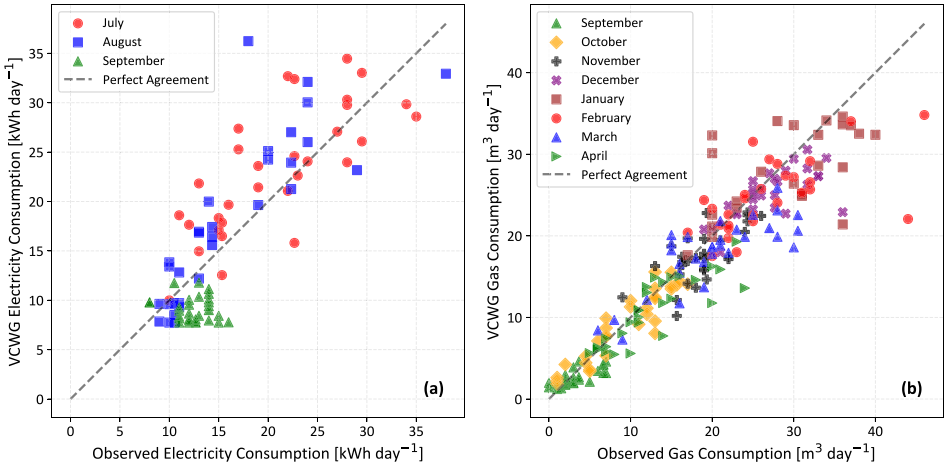

Fig. 11. Observed versus VCWG-simulated daily energy consumption across seasons: (a) electricity and (b) gas. The dashed 1:1 line denotes perfect agreement between simulations and observations. Points above the line indicate overestimation, while points below indicate underestimation. The gas panel covers September 2025 through April 2026 to capture the full heating-season progression and shoulder-season decline.

toward lower shoulder-season gas use. In addition to aggregate energy agreement, we evaluate whether VCWG reproduces the underlying indoor and envelope state variables that govern heating and cooling demand. This strengthens confidence that the VCWG setup, when driven by measured outdoor conditions and coupled with the indoor control behavior validated in the following section, can represent the building's operational energy response at the hourly and daily timescales.

As an additional contextual check of local representativeness, measured electricity and natural gas consumption from two nearby Guelph buildings with the same archetype were normalized by floor area and compared with the simulated representative building. The comparison showed that VCWG generally followed the magnitude and seasonal pattern of nearby measured electricity and gas use intensities, supporting the representativeness of the selected building within this local archetype. In addition, previous VCWG validation for a 29-premise residential neighborhood in London, Ontario showed close agreement in annual gas-use intensity and reproduced the observed seasonal pattern of monthly electricity consumption [31]. These contextual comparisons support local and cold-climate representativeness, but they do not replace the need for broader validation across building types, HVAC systems, climates, and urban morphologies.

3.1.2. Targeted comparison with VCWG v3.0.0 and EnergyPlus v26-1-0

A targeted monthly benchmark was added to compare VCWG v3.1.0 with both the previous VCWG v3.0.0 formulation and EnergyPlus v26-1-0. Fig. 12 compares observed monthly electricity and natural gas consumption with VCWG v3.1.0, VCWG v3.0.0, and EnergyPlus v26-1-0 over the July 2025–April 2026 validation period. Fig. 13 compares the sensible heating/cooling loads from the three simulations.

For electricity consumption, VCWG v3.1.0 improves the summer cooling-season agreement relative to VCWG v3.0.0. In July 2025 and August 2025, VCWG v3.0.0 substantially overpredicts electricity consumption, while VCWG v3.1.0 remains closer to the observations and also shows smaller overprediction than EnergyPlus v26-1-0. From September 2025 through April 2026, all three models underpredict measured electricity use, with broadly similar errors during much of the heating season. This common underprediction suggests that a substantial part of the measured non-cooling electricity consumption is associated with plug loads, lighting, equipment schedules, or operational details that were not fully represented in any of the simulation setups. Therefore, the heating-season electricity discrepancy should not be interpreted as a limitation unique to VCWG v3.1.0.

For natural gas consumption, all three models reproduce the seasonal increase from the shoulder season into winter and the decline toward spring. However, VCWG v3.1.0 generally provides smaller deviations from observations than both VCWG v3.0.0 and EnergyPlus v26-1-0, especially during the main heating and late heating-season months. EnergyPlus v26-1-0 tends to overpredict gas consumption across nearly the full validation period, while VCWG v3.1.0 remains closer to the observed values in most months.

Overall, the benchmark supports two conclusions. First, relative to VCWG v3.0.0, VCWG v3.1.0 provides improved monthly energy agreement in this case study, particularly for cooling-season electricity and heating-season natural gas. This supports the value of the new prognostic indoor heat and moisture formulation, revised HVAC sensible and latent capacity constraints, dynamic cooling COP treatment, and comfort-related control structure. Second, relative to EnergyPlus v26-1-0, VCWG v3.1.0 provides comparable or better monthly agreement for several energy-use patterns, especially natural gas consumption, while retaining internally coupled indoor heat and moisture dynamics, HVAC operation, comfort evaluation, and urban microclimate feedback.

3.1.3. One-factor-at-a-time sensitivity analysis

A one-factor-at-a-time sensitivity analysis was added to quantify how selected uncertain parameters affect monthly electricity and natural gas predictions. The analysis was performed for January 2026 and August 2025 to represent heating- and cooling-season operations, respectively. The tested parameters were infiltration rate, internal heat gains, and HVAC control setpoints. These parameters were selected because they directly affect air exchange, internal load magnitude, and thermostat-driven heating and cooling demand.

Fig. 14 shows the sensitivity of monthly electricity and gas consumption to infiltration rate. In January 2026, increasing infiltration substantially increases natural gas consumption, confirming that heating-season gas use is strongly controlled by air-exchange losses. January 2026 electricity remains nearly unchanged because heating is primarily gas-driven in the present configuration. In August 2025, electricity consumption increases with infiltration rate, while gas use remains close to zero, which is consistent with higher cooling load caused by greater exchange with warm outdoor air during the cooling season.

Fig. 15 shows the sensitivity to HVAC control setpoints. In January 2026, increasing the heating setpoint increases monthly gas consumption, as expected because a higher indoor temperature target increases the indoor-outdoor temperature difference and heating demand. In

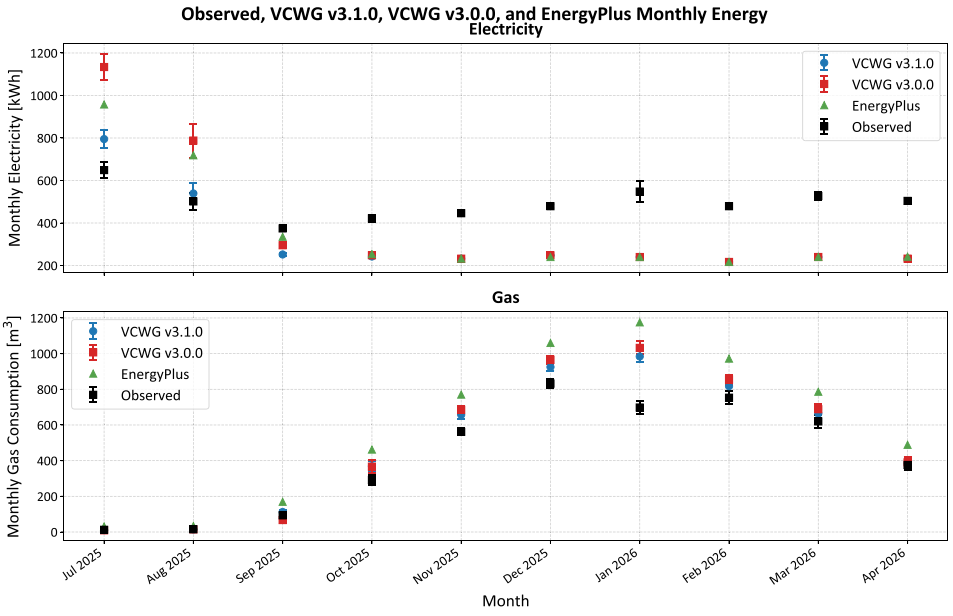

Fig. 12. Monthly electricity and natural gas consumption from observations, VCWG v3.1.0, VCWG v3.0.0, and EnergyPlus v26-1-0 over the July 2025–April 2026 validation period.

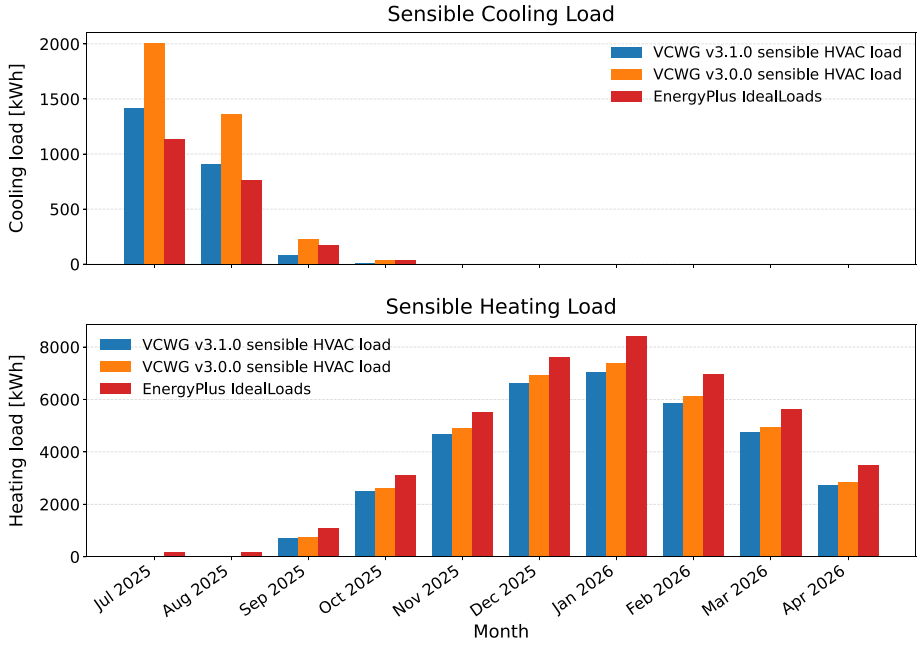

Fig. 13. Monthly sensible heating/cooling loads from observations, VCWG v3.1.0, VCWG v3.0.0, and EnergyPlus v26-1-0 over the July 2025–April 2026 validation period.

August 2025, increasing the cooling setpoint reduces monthly electricity consumption because the cooling system operates less aggressively. This result confirms that HVAC control assumptions are among the most influential operational parameters for monthly energy prediction.

Fig. 16 shows the sensitivity to total internal heat gain. Monthly electricity consumption increases with internal heat gain in both January 2026 and August 2025, reflecting the direct contribution of internal electric loads and the additional cooling burden during warm conditions. In contrast, natural gas consumption shows limited sensitivity to internal heat gain over the tested range. This indicates that, for the present case study, monthly gas consumption is more strongly governed by heating setpoint and infiltration rate than by the tested internal-gain range.

Overall, the sensitivity analysis shows that the dominant parameter influence depends on season and end use. Heating-season gas consumption is most sensitive to infiltration rate and heating setpoint, while cooling-season electricity consumption responds strongly to cooling setpoint, internal gains, and infiltration rate. These results provide additional support for the validation by identifying which assumptions most strongly influence the monthly energy predictions and by showing that the model responds physically to key building and control parameters.

3.1.4. Scope and generalizability of the validation

The present validation focuses on the HVAC configuration and model framework available in the monitored representative building. However,

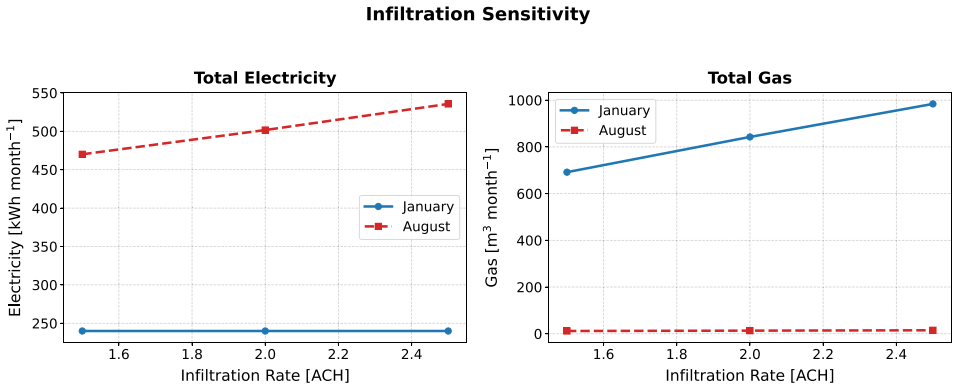

Fig. 14. One-factor-at-a-time sensitivity of monthly electricity and natural gas consumption to infiltration rate for representative heating-season (January 2026) and cooling-season (August 2025) periods.

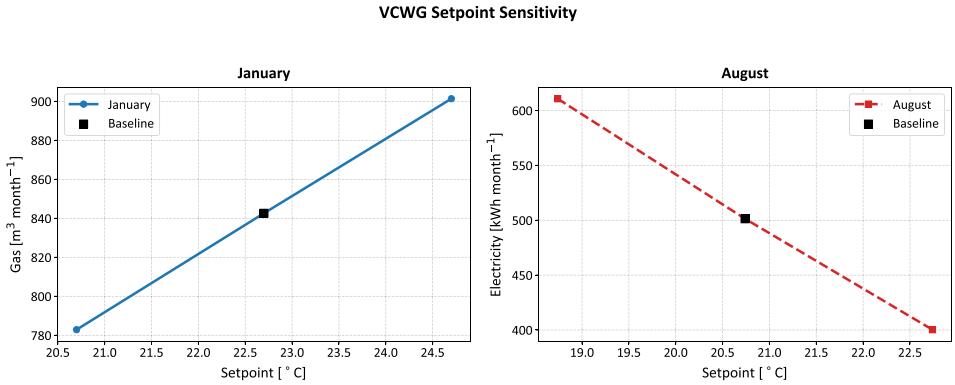

Fig. 15. One-factor-at-a-time sensitivity of January (2026) natural gas consumption to heating setpoint and August (2025) electricity consumption to cooling setpoint. Baseline markers indicate the setpoints used in the validation simulation.

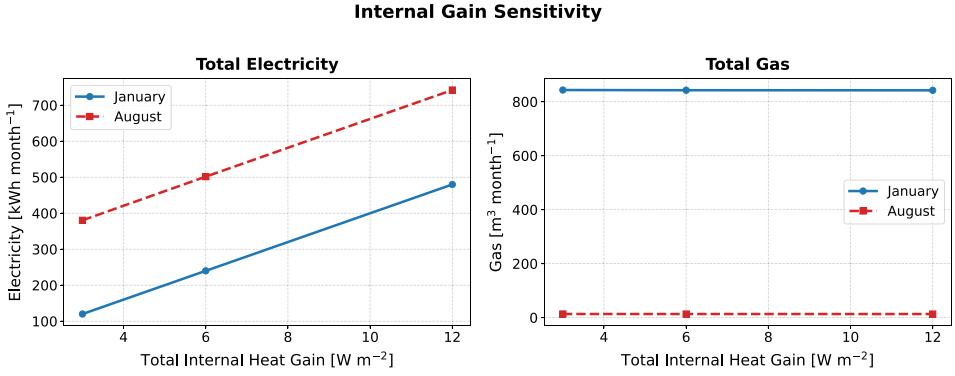

Fig. 16. One-factor-at-a-time sensitivity of monthly electricity and natural gas consumption to total internal heat gain for representative heating-season (January 2026) and cooling-season (August 2025) periods.

the VCWG platform itself is not restricted to this single configuration and has previously been extended to represent alternative building energy systems, including heat pumps, heat recovery, renewable systems, building-integrated thermal energy storage, and phase change materials. Therefore, the limitation of the present study is not the general modeling scope of VCWG, but the fact that the proposed HVAC model was field-validated for one monitored HVAC configuration. Additional validation across other HVAC system types remains necessary [27,31].

Urban morphology can influence local microclimate, envelope heat exchange, and HVAC demand. This dependence is one motivation for using VCWG, because the model explicitly represents urban canyon geometry, vegetation, radiation exchange, vertical diffusion, building energy exchange, and indoor–outdoor feedback. Previous VCWG applications have included urban settings with different Local Climate Zone (LCZ) characteristics, including denser European street-canyon morphologies, mid-rise urban forms, and more open North American low-rise neighborhoods. Therefore, the present Guelph case should be interpreted as a local field validation of the proposed HVAC model framework, while the broader VCWG platform has been applied across a wider range of urban morphology types.

Although the extended monitoring period, normalized comparison with nearby buildings, and previous VCWG applications improve

Table 6
Monthly and pooled hourly performance metrics comparing VCWG simulations with observed indoor air temperature, indoor relative humidity, and interior surface temperatures measured with the wall and ceiling thermocouples (Fig. 4). Metrics are computed at the hourly time step. The table reports calculable monthly Pearson's correlation values, including weak or negative values, and to add pooled Pearson's correlation coefficients across the full July 2025–April 2026 monitoring period.

Period	In. Air Temp. [°C]			In. RH [%]			Wall Surf. Temp. [°C]			Ceil. Surf. Temp. [°C]		
	Bias	$RMSE$	r	Bias	$RMSE$	r	Bias	$RMSE$	r	Bias	$RMSE$	r
Jul	0.058	0.332	0.264	4.260	9.840	0.229	0.583	0.761	0.644	1.122	1.241	0.768
Aug	−0.353	1.169	0.708	3.538	12.062	0.415	0.335	1.054	0.853	0.341	0.784	0.929
Sep	0.356	0.965	0.073	−1.714	8.665	0.733	1.027	1.430	−0.109	−0.651	1.552	−0.419
Oct	0.343	0.632	0.050	−2.067	5.144	0.867	1.289	1.391	0.610	−2.776	3.267	−0.285
Nov	0.512	0.540	0.058	−0.708	2.404	0.842	1.985	2.041	0.545	−5.117	5.306	0.496
Dec	−0.154	0.207	0.190	−1.566	2.536	0.906	1.974	2.067	0.267	−7.217	7.405	0.264
Jan	0.033	0.431	0.239	−1.395	2.205	0.968	2.440	2.659	0.497	−7.723	7.951	0.521
Feb	−0.203	0.734	0.188	−0.494	2.033	0.938	2.629	2.934	0.242	−7.146	7.354	0.409
Mar	−0.214	0.325	0.006	−0.353	5.943	0.854	2.083	2.297	0.244	−5.562	5.776	0.330
Apr	−0.585	0.751	−0.250	−0.037	9.368	0.842	1.218	1.389	0.583	−3.924	4.182	0.750
All months pooled	**−0.020**	**0.672**	**0.720**	**−0.038**	**7.014**	**0.950**	**1.547**	**1.913**	**0.740**	**−3.840**	**5.145**	**0.002**

Monthly Pearson's correlation values should be interpreted cautiously during low-variance periods.

confidence in the local representativeness of the results, the present validation should not be interpreted as a universal validation across all building typologies, HVAC systems, climates, or Local Climate Zones (LCZ). The results support the monitored Guelph case and provide a methodological demonstration of the proposed prognostic HVAC and comfort-control framework. Broader validation across multiple building types, HVAC configurations, climates, and urban morphologies remains necessary before generalizing the proposed HVAC model.

3.2. Time series model performance evaluation

Table 6 presents the corresponding monthly performance metrics computed at the hourly time resolution for indoor air temperature, indoor relative humidity, and interior surface temperatures. Indoor air temperature is tightly regulated by thermostat control, which compresses the observed dynamic range and makes Pearson's correlation highly sensitive to small phase shifts and measurement noise. Under these conditions, r is easy to misinterpret and does not track absolute agreement. Therefore, indoor air temperature correlations are reported where calculable, but interpreted cautiously, and the evaluation emphasizes Bias and $RMSE$. For variables with broader and more physically driven variability, especially indoor relative humidity and envelope surface temperatures, r remains a useful secondary indicator of pattern timing.

Hourly indoor air temperature results demonstrate consistently strong performance across the July 2025–April 2026 validation period. $RMSE$ remains below 1.2 °C throughout the study period. Bias remains small in magnitude, ranging from −0.585 °C to +0.512 °C, indicating that VCWG reproduces indoor air temperature levels without systematic drift. The pooled correlation for indoor air temperature is $r = 0.720$, indicating that the model captures the broader temporal pattern across the full monitoring period, even though month-specific correlations can be weak under thermostat-limited variability.

Hourly relative humidity shows the largest deviations during summer months and in April 2026, followed by sustained improvement through much of the heating season. In July 2025 and August 2025, VCWG results for indoor relative humidity fluctuate around the setpoint due to high variations in outdoor humidity dynamics during the summer, leading to Bias values of +4.260% and +3.538% with $RMSE$ values near 10 to 12%. From September 2025 through March 2026, bias becomes slightly negative, ranging from −1.714% to −0.353% and $RMSE$ drops substantially, reaching its lowest value in February 2026 ($RMSE = 2.03\%$). April 2026 shows a near-zero mean bias (−0.037%) but a higher $RMSE$ of 9.368%. Correlation for relative humidity is strong from September 2025 onward ($r = 0.73$ to 0.97), and the consistently high values from September 2025 to April 2026 indicate that VCWG captures the timing and temporal evolution of indoor humidity well during the heating and shoulder-season periods. The pooled relative humidity correlation is also strong ($r = 0.950$), supporting the model's ability to capture the overall hourly humidity pattern across the full validation period.

Interior surface temperatures measured by the wall and ceiling thermocouples (Fig. 4) show a clear seasonal structure that complements the indoor air validation. Wall surface temperatures exhibit a positive bias across all months, indicating that VCWG generally predicts warmer wall surface temperatures than measured. $RMSE$ ranges from 0.761 °C in July 2025 to 2.934 °C in February 2026. March 2026 and April 2026 show wall surface temperature Bias values of +2.083 °C and +1.218 °C, respectively. Correlation is strongest in July 2025, August 2025, October 2025, and April 2026 ($r = 0.583$ to 0.853), while lower or negative correlations in some months indicate that local surface heat exchange, sensor placement, and reduced dynamic range affect temporal agreement. Across the full monitoring period, the pooled wall surface temperature correlation is $r = 0.740$, indicating good overall temporal agreement despite month-to-month variability.

Ceiling surface temperatures are more challenging to reproduce, particularly in the winter. The model overestimates ceiling temperature in July 2025 and August 2025 with Bias values of +1.122 °C and +0.341 °C, respectively, then shifts to an increasingly cool bias from September onward. The negative bias reaches −7.217 °C in December 2025, −7.723 °C in January 2026, and −7.146 °C in February 2026. March 2026 and April 2026 show reduced but still negative ceiling surface temperature Bias values of −5.562 °C and −3.924 °C, respectively. The corresponding $RMSE$ increases during winter and decreases again in April 2026. Ceiling surface temperature correlation remains high in the summer, from July 2025 to August 2025, with $r = 0.768$ to 0.929, and improves again in April 2026 with $r = 0.750$. September 2025 and October 2025 ceiling surface temperature correlations are reported for transparency but are not interpreted as meaningful pattern agreement because the computed values are negative, with $r = -0.419$ and $r = -0.285$, respectively. The pooled ceiling surface temperature correlation is weak, with $r = 0.002$, mainly because the pooled coefficient reflects both within-month temporal tracking and between-month seasonal consistency. The observed ceiling surface temperature remains relatively stable across the monitoring period because of indoor thermal regulation, while the simulated ceiling surface temperature shows a strong heating-season offset. Therefore, the near-zero pooled correlation is interpreted primarily as evidence of seasonal inconsistency in the simulated ceiling surface temperature level, rather than a complete absence of within-month temporal agreement. This overall behavior suggests that ceiling surface temperatures are more sensitive to localized radiant exchange, vertical stratification near the ceiling, and envelope parameter uncertainty.

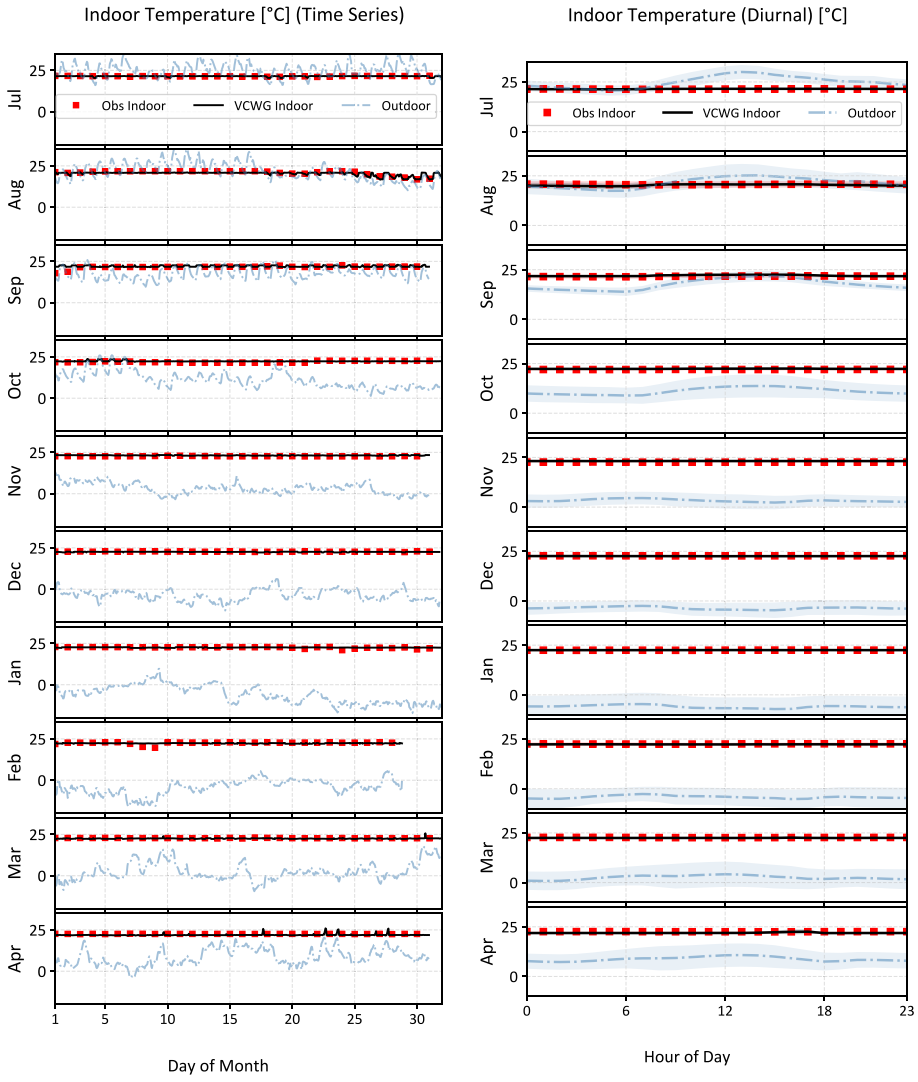

(a) Hourly indoor air temperature time series.

(b) Mean diurnal indoor air temperature profile.

Fig. 17. Comparison between observed and VCWG-simulated indoor air temperature for July 2025–April 2026. Panel (a) shows hourly temperature time series with day of month on the horizontal axis, while panel (b) shows mean diurnal temperature profiles aggregated over each month ± one standard deviation. Outdoor temperature is included where available for contextual reference.

Fig. 17 evaluates how well VCWG reproduces the measured indoor air temperature for July 2025–April 2026 when driven by the observed outdoor conditions. The comparison is shown in two complementary views: the full hourly evolution in Fig. 17(a) and the mean diurnal profile in Fig. 17(b). Together, these plots test both time series tracking (hourly agreement through weather events and seasonal transitions) and systematic behavior (persistent diurnal bias or amplitude errors).

In Fig. 17(a), the observed indoor temperature (red squares) remains tightly controlled around a nearly constant level across all months, even as outdoor temperature (blue dashed) changes substantially from the summer to the spring shoulder season. This pattern is consistent with active HVAC control maintaining a setpoint. The VCWG indoor temperature (black) follows the measurements with near overlap throughout the study period, indicating that the model reproduces the controlled indoor conditions under realistic forcing. Importantly, the agreement holds not only during relatively steady periods but also across short-term outdoor fluctuations, suggesting that the modeled building thermal response and control logic are behaving consistently. From July 2025 through early September 2025, outdoor temperatures are higher and more variable, yet the indoor series stays stable and VCWG tracks it closely. As the season progresses into October 2025, November 2025, December 2025, January 2026, and February 2026, outdoor temperatures drop markedly and the contrast between indoor and outdoor temperatures increases, while the indoor series remains steady and continues to be reproduced by VCWG without visible drift. In March 2026 and April 2026, outdoor temperatures begin to rise again, but the indoor temperature remains controlled and the simulated indoor series continues to follow the measured values closely. A modest shift in the indoor level and slightly increased short-term variability in late August 2025 is also reflected by the model, which indicates that the simulation can capture small changes in the indoor operating condition rather than producing a fixed, overly idealized indoor trajectory.

Fig. 17(b) provides a structured check of diurnal behavior by averaging each month across the hour of day. This view is useful because small systematic errors can be hard to detect in the hourly plots but become clear when aggregated. The observed indoor temperature shows an almost flat diurnal profile in every month, with only minor hour-to-hour variation. VCWG reproduces both the mean level and the very weak diurnal amplitude, with the simulated curve closely aligned to the observed points across the entire 24-hour cycle. In contrast, the outdoor

temperature exhibits a clear diurnal cycle in the summer, with a daytime peak and nighttime minimum that is strongest in July 2025 and August 2025, weakens through September 2025 and October 2025, and becomes much smaller in November 2025, December 2025, January 2026, and February 2026. The outdoor diurnal cycle becomes more visible again in March 2026 and April 2026 as outdoor conditions transition toward spring, while the indoor diurnal profile remains comparatively stable. The indoor series does not mirror that outdoor cycle, which is expected for a conditioned space, and VCWG reproduces this decoupling correctly. The lack of a noticeable phase shift or amplitude bias in the indoor diurnal curves indicates that the model does not artificially amplify outdoor-driven fluctuations indoors, nor does it introduce a persistent timing error associated with thermal inertia or control response.

Overall, Fig. 17(a) and (b) show that VCWG captures both the instantaneous indoor temperature evolution and the aggregated diurnal characteristics over a multi-month period spanning summer, winter, and shoulder-season conditions. This temperature agreement supports the credibility of the subsequent energy validation, because it indicates that the model maintains realistic indoor operating conditions while responding to measured outdoor forcing.

Fig. 18 shows the hourly and mean diurnal interior wall surface temperatures. As noted earlier, the simulated wall temperatures show a warm bias across the validation period. Furthermore, there is a small diurnal variability that is visible in both the model output and the measurements.

Fig. 19 shows the hourly and mean diurnal indoor relative humidity. The model skill in maintaining the indoor relative humidity setpoint is very good. In the cooling season (July 2025, August 2025, and September 2025) a diurnal cycle in relative humidity is observed, likely due to outdoor fluctuations (night-time high relative humidity and day-time low relative humidity). However, the amplitude of such diurnal variability is damped during the heating season and shoulder-season months. The March 2026 and April 2026 profiles show that the model continues to capture the main humidity pattern as outdoor conditions transition toward spring, although April 2026 shows larger short-term variability around a near-zero mean bias. Overall, the VCWG model does not exhibit a substantial bias in predicting the indoor relative humidity.

Fig. 20 illustrates the validation of the model's surface temperature predictions for the roof and northeast wall over a 24-hour period on December 21, 2025. The continuous curves depict the simulated results from the VCWG model, while the overlaid thermal images provide independent empirical verification at four-hour intervals (00:00, 04:00, 08:00, 12:00, 16:00, 20:00 local time). As shown in the figure, the wall temperatures (red markers) are reproduced more consistently than the roof (blue markers). For the wall, the simulation predicts a diurnal cycle in exterior wall temperature, which the observations do not suggest. The largest mismatch occurs around midday where the simulated wall is warmer by roughly 5°C. In contrast, the roof exhibits larger and more systematic offsets, with errors on the order of several degrees during the night and early morning and reaching nearly 10°C around noon. This behavior is consistent with the roof being strongly controlled by radiative exchange with the sky and by uncertain surface optical properties, such as emissivity [46]. The thermal image of the roof indicates large temperature variations of up to 10°C, which makes the measurement uncertain. Overall, the biases in the exterior surface temperatures are compensated by convective heat transfer coefficient parameterizations in VCWG, so that the building heat loss or gain are not under-predicted or over-predicted.

3.3. Observed predicted mean vote (PMV) behavior and physical drivers

Fig. 21 compares the hourly PMV time series and mean diurnal PMV profile between Ladybug-derived observations and VCWG output across the summer, winter, and shoulder months from July 2025 to April 2026. Panel (a) shows the hourly PMV evolution, while panel (b)

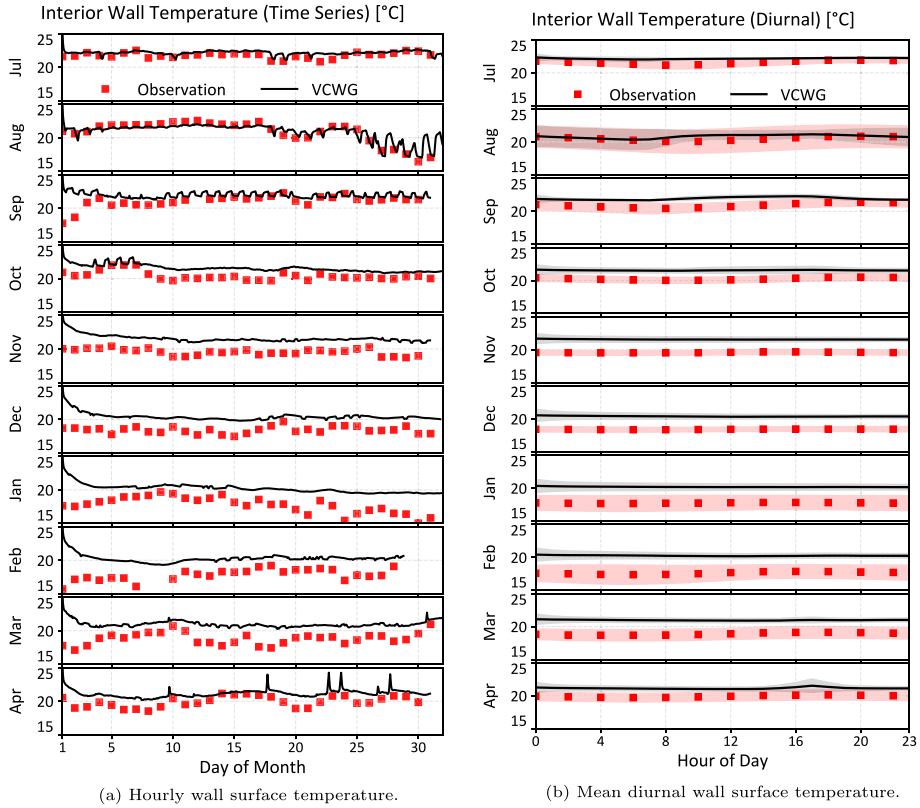

(a) Hourly wall surface temperature.

(b) Mean diurnal wall surface temperature.

Fig. 18. Wall surface temperature validation for July 2025–April 2026. The black line represents the VCWG simulation, while red markers show the thermocouple observations. Diurnal profiles (b) include shaded uncertainty bands for both simulated and measured data (± one standard deviation). (For interpretation of the references to colour in this figure legend, the reader is referred to the web Version of this article.)

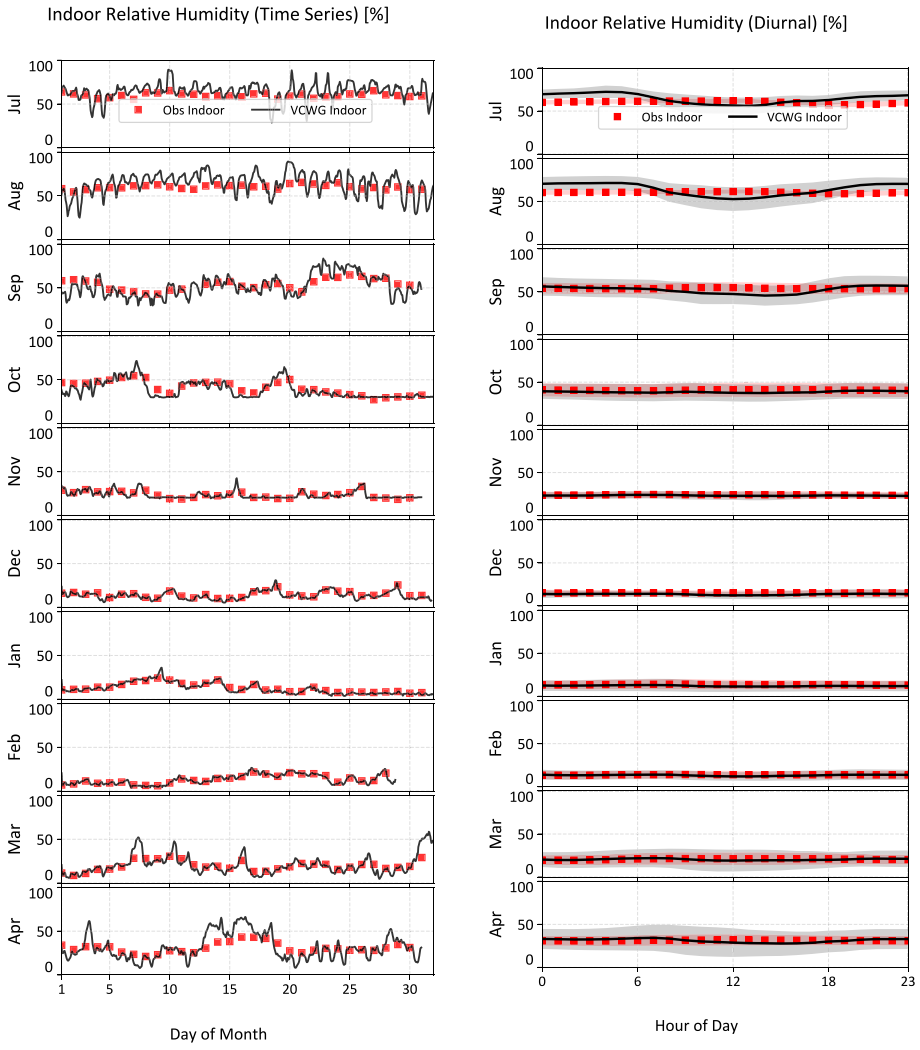

(a) Hourly indoor relative humidity time series. (b) Mean diurnal indoor relative humidity profile.

Fig. 19. Comparison between observed and VCWG-simulated indoor relative humidity for July 2025–April 2026. Panel (a) shows hourly humidity time series with day of month on the horizontal axis, while panel (b) shows mean diurnal humidity profiles ± one standard deviation aggregated over each month.

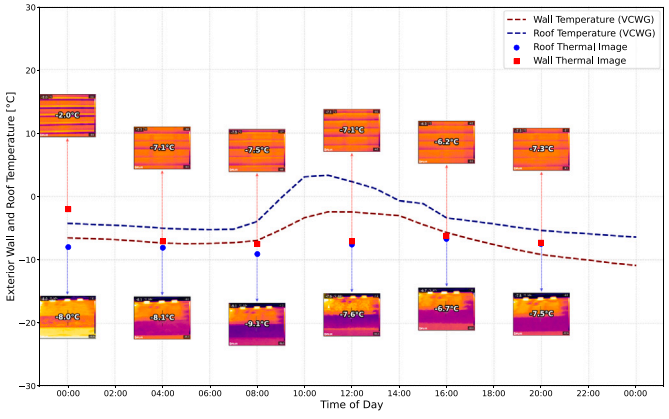

Fig. 20. Validation of modeled exterior surface temperature against observed exterior mean surface temperature by thermal imaging. Comparison of simulated (VCWG) and observed surface temperatures for the roof and northeast wall on 21 December 2025.

shows the mean diurnal PMV profile with shaded bands representing mean ± one standard deviation. The results show that PMV remains persistently negative throughout the day with only weak diurnal variation, consistent with a mechanically conditioned space where indoor air temperature is regulated and does not swing strongly within a day. VCWG reproduces the small temporal variations reasonably well, but both the observations and simulations indicate that the indoor environment is systematically cool in terms of PMV even when the thermostat maintains a stable air temperature.

The measured indoor conditions help explain this result. The PMV was calculated using all required environmental variables obtained from indoor sensors, including indoor air temperature, relative humidity, mean radiant temperature, and air velocity. The metabolic rate was kept constant at 1.2 met, representing light office-type activity, while clothing insulation was assigned seasonally, with $clo = 0.5$ for warm months and $clo = 1.0$ for cold months. For the winter case discussed here, $clo = 1.0$ was used. During the measured winter period (e.g., 1 December 2025), the indoor air temperature is tightly controlled at $T_{in} \approx 22.7$–22.8 °C, while the MRT remains slightly lower at $T_{mrt} \approx 22.0$ °C.

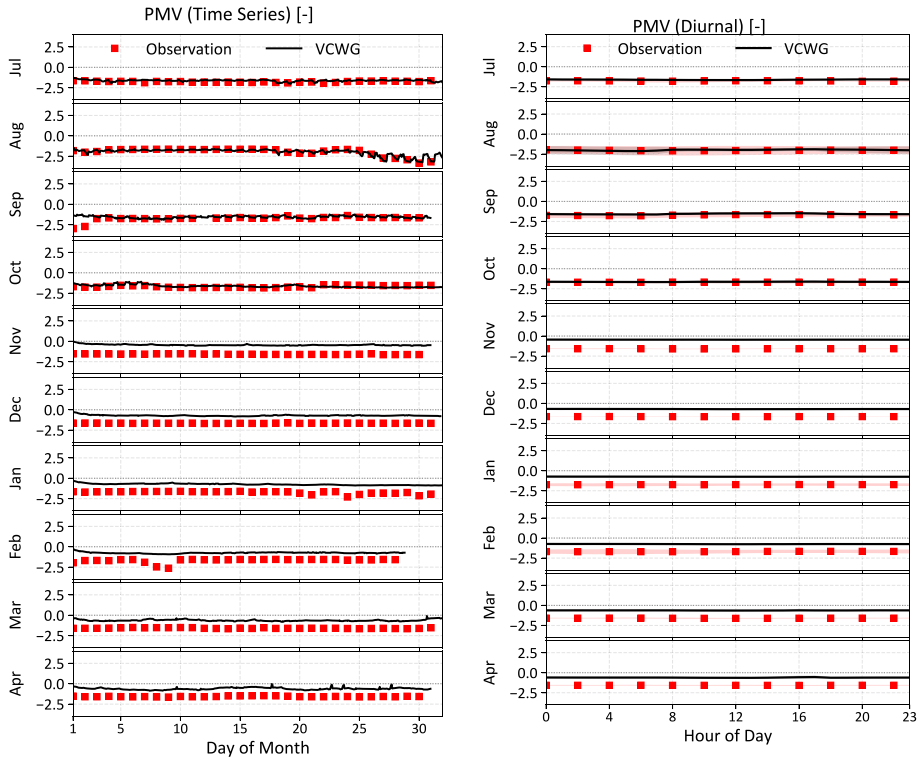

(a) Hourly PMV time series. (b) Mean diurnal PMV profile.

Fig. 21. Predicted mean Vote (PMV) comparison between Ladybug-derived observations and VCWG output from July 2025 to April 2026. Values near zero indicate neutral thermal sensation, with the shaded bands in (b) illustrating the changes in comfort levels throughout the diurnal cycle (mean ± one standard deviation).

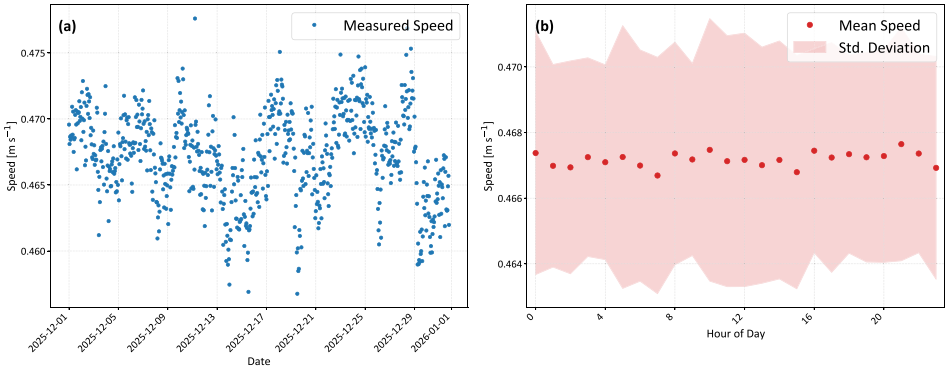

Fig. 22. Measured indoor air speed for December 2025 ((a) time series and (b) diurnal mean ± one standard deviation).

Relative humidity is very low (RH ≈ 15–17%), but, within the Fanger formulation, humidity typically has a weaker effect on PMV than operative conditions and air movement at these temperatures. In contrast, as shown in Fig. 22, the measured indoor air speed is consistently high for an occupied zone (≈ 0.47 m s^{-1}). The anemometer was not positioned directly in a ventilation channel or supply air path, and the nearby wall is an interior partition rather than an exterior corner. The sensor location was selected to support stable long-term monitoring in an occupied office space. Such air motion increases convective heat loss from the body and can drive PMV to strongly negative values even when T_{in} and T_{mrt} are near conventional heating setpoints. The small but persistent $T_{in} - T_{mrt}$ offset further contributes through reduced MRT, which is consistent with the broader observation of cool interior surfaces in the winter, particularly when wall temperatures drop and lower the radiant field experienced by occupants.

Although the calculated PMV values were low, they should not be interpreted as direct evidence of occupant discomfort. Occupant behavior provides important context. Despite the low PMV values shown in Fig. 21, occupants did not increase heating setpoints during winter, which suggests that the indoor conditions were acceptable in practice. This apparent difference between PMV-based assessment and observed occupant response may reflect adaptive behavior, such as wearing heavier clothing at certain times, changes in activity level, or acclimatization to slightly cooler indoor conditions. Therefore, in this case, the low PMV values mainly indicate that the measured indoor environment promoted greater heat loss from occupants, due primarily to elevated air speed and slightly lower radiant temperature, rather than demonstrating that occupants necessarily perceived the space as uncomfortable.

4. Conclusion

The primary outcome of this research was the development and validation of VCWG v3.1.0, a unified internally coupled single-solver modeling framework in which indoor temperature and specific humidity evolve as prognostic state variables while remaining natively coupled to a multi-physics urban canyon model. The framework was evaluated against a July 2025–April 2026 period of high-resolution, co-located measurements from an instrumented building in Guelph, Ontario, with simulations forced by on-site outdoor observations. A targeted monthly energy benchmark against VCWG v3.0.0 and EnergyPlus v26-1-0 was also included to evaluate the advancement of VCWG v3.1.0 within the VCWG model family and to provide an external reference for predicted electricity and natural gas consumption under comparable input assumptions. The key findings are summarized below:

1. VCWG v3.1.0 establishes a practical middle ground between indoor-focused building energy simulators and outdoor-focused urban microclimate tools. By resolving the prognostic canyon microclimate alongside indoor heat and moisture states and an active HVAC response, the framework evaluates the fully coupled indoor–outdoor system within a single computational environment, reducing the synchronization, data-exchange, and timescale-management challenges associated with external co-simulation. This internal coupling is intended as a computationally efficient framework for long-duration comfort, humidity, HVAC, and urban microclimate studies, rather than a universal replacement for high-fidelity external co-simulation when detailed multi-zone building physics are required.
2. The prognostic formulation reproduces hourly indoor conditions with high fidelity across the multi-month simulation period. The model maintains a Root Mean Square Error ($RMSE$) of 0.7 °C for indoor air temperature and 7% for relative humidity.
3. The framework captures seasonal energy regime transitions, demonstrating robust agreement for cooling-dominated electricity variability in summer and heating-dominated natural gas consumption in winter and the shoulder-season transition.
4. Independent envelope checks indicate that the largest remaining thermal mismatches occur on sky-exposed surfaces. Even when indoor air temperature error is low, thermal imaging shows closer agreement for external wall surfaces than for roof surfaces, identifying radiative boundary conditions and roof surface parameterization as dominant sensitivities.
5. The native two-way coupling enables physically consistent indoor–outdoor feedback analysis. The framework captures how sensible and latent heat rejected by the HVAC system modifies canyon microclimate states and how those modified states feed back into building thermal loads.
6. The targeted monthly benchmark shows that VCWG v3.1.0 improves monthly energy agreement relative to VCWG v3.0.0, particularly for cooling-season electricity and heating-season natural gas consumption, while also providing comparable or smaller deviations than EnergyPlus v26-1-0 for several monthly energy-use patterns in this case study.
7. By explicitly resolving indoor specific humidity rather than relying on static load assumptions, the model provides a credible basis for evaluating occupant comfort. Comfort indices that depend on transient moisture cycles can be interpreted with greater confidence than dry-bulb setpoint tracking alone.
8. This validation establishes a basic foundation for neighborhood-scale and urban-scale digital twin applications. Demonstrated performance under measured forcing supports observation-driven tracking of building states and enables quantitative “what-if” testing for operational optimization and climate resilience strategies.

4.1. Recommendations for future work

Recommendations for future work include:

1. Extend validation beyond this study by testing additional building types, HVAC configurations, climates, operational typologies, and urban morphologies, followed by district-scale simulations to quantify aggregate sensible and latent heat feedback on canyon microclimate conditions.
2. Reduce uncertainty in roof and ceiling performance by refining radiative exchange and boundary condition treatments and by better constraining surface optical properties and convective heat transfer coefficients, particularly for sky-exposed surfaces.
3. Improve operational realism by incorporating occupant-driven schedules and calibrated internal gains, and by evaluating alternative control strategies, including adaptive comfort-based thermostat logic.
4. Develop an updatable digital twin workflow that integrates calibration and state updating with streaming sensor inputs, allowing key indoor and canyon states, along with associated uncertainties, to evolve over time for real-time control and retrofit evaluation.
5. Benchmark VCWG v3.1.0 against external VCWG–EnergyPlus co-simulation workflows for representative low-rise, mid-rise, and high-rise buildings to quantify trade-offs among accuracy, computational cost, synchronization requirements, and building-system detail.

CRediT authorship contribution statement

Mojtaba Safdari: Writing – review & editing, Writing – original draft, Software, Methodology, Investigation, Data curation, Conceptualization. **M. Nauman Ashraf:** Writing – review & editing, Writing – original draft, Data curation. **Mohammad Al Janaideh:** Writing – review & editing, Supervision. **Kamran Siddiqui:** Writing – review & editing, Writing – original draft, Supervision, Funding acquisition. **Amir A. Aliabadi:** Writing – review & editing, Writing – original draft, Visualization, Validation, Supervision, Software, Methodology, Investigation, Funding acquisition, Formal analysis, Data curation.

Declaration of Generative AI and AI-assisted technologies in the writing process

During the preparation of this work, the author(s) used GPT-5 in order to typeset figures, tables, and equations. After using this tool/service, the author(s) reviewed and edited the content as needed and take(s) full responsibility for the content of the publication.

Declaration of competing interest

The authors declare that they have no known competing financial interests or personal relationships that could have appeared to influence the work reported in this paper.

Acknowledgements

The authors would like to thank Ali Madadizadeh, Yusra Hasan, and Iman Sekhavati for their valuable support and contributions to this work. This research was supported by the University of Guelph through the International Doctoral Tuition Scholarship (IDTS); Braithwaite Travel Award; the Discovery Grant program (401231) from the Natural Sciences and Engineering Research Council (NSERC) of Canada; and the Climate Action and Awareness Fund (CAAF) (055725) from Environment and Climate Change Canada (ECCC).

Data availability

The Atmospheric Innovations Research (AIR) Laboratory at the University of Guelph provides the model source code. For access, contact Amir A. Aliabadi (aaliabad@uoguelph.ca), visit http://www.aaa-scientists.com/, or visit https://github.com/AmirAAliabadi.

References

[1] A. Worthy, M. Ashayeri, J. Marshall, N. Abbasabadi, Bridging the simulation-to-reality gap: a comprehensive review of microclimate integration in urban building energy modeling (UBEM), Energy Build. (2025) 115392, https://doi.org/10.1016/j.enbuild.2025.115392

[2] F. Salamanca, A. Krpo, A. Martilli, A. Clappier, A new building energy model coupled with an urban canopy parameterization for urban climate simulations–Part I. formulation, verification, and sensitivity analysis of the model, Theor. Appl. Climatol. 99 (2010) 331–344, https://doi.org/10.1007/s00704-009-0142-9

[3] L. Wang, L. Wu, L.K. Norford, A.A. Aliabadi, E. Lee, The interactive indoor-outdoor building energy modeling for enhancing the predictions of urban microclimates and building energy demands, Build. Environ. 248 (2024) 111059, https://doi.org/10.1016/j.buildenv.2023.111059

[4] L. Pasandi, Z. Qian, W.L. Woo, Quantifying urban microclimate feedback on building energy use using a coupled simulation workflow, Build. Environ. (2025) 113657, https://doi.org/10.1016/j.buildenv.2025.113657

[5] N. Sezer, H. Yoonus, D. Zhan, L.L. Wang, I.G. Hassan, M.A. Rahman, Urban microclimate and building energy models: a review of the latest progress in coupling strategies, Renew. Sustain. Energy Rev. 184 (2023) 113577, https://doi.org/10.1016/j.rser.2023.113577

[6] J. Bouyer, C. Inard, M. Musy, Microclimatic coupling as a solution to improve building energy simulation in an urban context, Energy Build. 43 (7) (2011) 1549–1559, https://doi.org/10.1016/j.enbuild.2011.02.010

[7] L. Chen, E. Ng, Outdoor thermal comfort and outdoor activities: a review of research in the past decade, Cities 29 (2) (2012) 118–125, https://doi.org/10.1016/j.cities.2011.08.006

[8] P.A. Mirzaei, Recent challenges in modeling of urban heat island, Sustain. Cities Soc. 19 (2015) 200–206, https://doi.org/10.1016/j.scs.2015.04.001

[9] M. Mosteiro-Romero, D. Maiullari, M. Pijpers-van Esch, A. Schlueter, An integrated microclimate-energy demand simulation method for the assessment of urban districts, Front. Built Environ. 6 (2020) 553946, https://doi.org/10.3389/fbuil.2020.553946

[10] P.J. Crank, D.J. Sailor, G. Ban-Weiss, M. Taleghani, Evaluating the ENVI-met microscale model for suitability in analysis of targeted urban heat mitigation strategies, Urban Clim. 26 (2018) 188–197, https://doi.org/10.1016/j.uclim.2018.09.002

[11] Y. Toparlar, B. Blocken, B. Maiheu, G.J.F. van Heijst, A review on the CFD analysis of urban microclimate, Renew. Sustain. Energy Rev. 80 (2017) 1613–1640, https://doi.org/10.1016/j.rser.2017.05.248

[12] S. Tsoka, A. Tsikaloudaki, T. Theodosiou, Analyzing the ENVI-met microclimate model's performance and assessing cool materials and urban vegetation applications: a review, Sustain. Cities Soc. 43 (2018) 55–76, https://doi.org/10.1016/j.scs.2018.08.009

[13] P.A. Mirzaei, F. Haghighat, Approaches to study urban heat island: abilities and limitations, Build. Environ. 45 (10) (2010) 2192–2201, https://doi.org/10.1016/j.buildenv.2010.04.001

[14] C.F. Reinhart, C.C. Davila, Urban building energy modeling: a review of a nascent field, Build. Environ. 97 (2016) 196–202, https://doi.org/10.1016/j.buildenv.2015.12.001

[15] F.M. Alves, A. Gonçalves, M.R. Del Caz-Enjuto, The use of envi-met for the assessment of nature-based solutions' potential benefits in industrial parks: a case study of argales industrial park (Valladolid, Spain), Infrastructures 7 (6) (2022) 85, https://doi.org/10.3390/infrastructures7060085

[16] D.B. Crawley, L.K. Lawrie, F.C. Winkelmann, W.F. Buhl, Y.J. Huang, C.O. Pedersen, R.K. Strand, R.J. Liesen, D.E. Fisher, M.J. Witte, Energyplus: creating a new-generation building energy simulation program, Energy Build. 33 (2001) 319–331, https://doi.org/10.1016/S0378-7788(00)00114-6

[17] Carrier Global Corporation, Hourly analysis program (HAP) v6.0, software, 2024, https://www.carrier.com/commercial/en/us/software/hvac-system-design/hap/.

[18] S.A. Klein, Trnsys-a transient system simulation program, Tech. rep., University of Wisconsin-Madison, Madison, 1988.

[19] Solar Energy Laboratory, University of Wisconsin-Madison, TRNSYS 18, software, 2017. http://www.trnsys.com.

[20] S. Attia, J.L.M. Hensen, L. Beltrán, A. De Herde, Selection criteria for building performance simulation tools: contrasting architects' and engineers' needs, J. Build. Perform. Simul. 5 (3) (2012) 155–169, https://doi.org/10.1080/19401493.2010.549573

[21] E. Erdogan, Comparative studies of building performance simulation tools (EnergyPlus, IES-VE, IDA-ICE) (Master's thesis), Politecnico Di Milano, Milano, 2020.

[22] D.B. Crawley, J.W. Hand, M. Kummert, B.T. Griffith, Contrasting the capabilities of building energy performance simulation programs, Build. Environ. 43 (4) (2008) 661–673, https://doi.org/10.1016/j.buildenv.2006.10.027

[23] M. Santamouris, On the energy impact of urban heat island and global warming on buildings, Energy Build. 82 (2014) 100–113, https://doi.org/10.1016/j.enbuild.2014.07.022

[24] M. Palme, L. Inostroza, G. Villacreses, A. Lobato-Cordero, C. Carrasco, From urban climate to energy consumption: enhancing building performance simulation by including the urban heat island effect, Energy Build. 145 (2017) 107–120, https://doi.org/10.1016/j.enbuild.2017.03.069

[25] T. Hong, Y. Chen, X. Luo, N. Luo, S.H. Lee, Ten questions on urban building energy modeling, Build. Environ. 168 (2020) 106508, https://doi.org/10.1016/j.buildenv.2019.106508

[26] B. Bueno, L. Norford, J. Hidalgo, G. Pigeon, The urban weather generator, J. Build. Perf. Simulat. 6 (4) (2012) 269–281, https://doi.org/10.1080/19401493.2012.718797

[27] M. Moradi, B. Dyer, A. Nazem, M.K. Nambiar, M.R. Nahian, B. Bueno, C. Mackey, S. Vasanthakumar, N. Nazarian, E.S. Krayenhoff, L.K. Norford, A.A. Aliabadi, The vertical city weather generator (VCWG v1.3.2), Geosci. Model Dev. 14 (2) (2021) 961–984, https://doi.org/10.5194/gmd-14-961-2021

[28] M. Moradi, E.S. Krayenhoff, A.A. Aliabadi, A comprehensive indoor–outdoor urban climate model with hydrology: the vertical city weather generator (VCWG v2.0.0), Build. Environ. 207 (2022) 108406, https://doi.org/10.1016/j.buildenv.2021.108406

[29] A.A. Aliabadi, M. Moradi, R.M. McLeod, D. Calder, R. Dernovsek, How much building renewable energy is enough? The vertical city weather generator (VCWG v1.4.4), Atmosphere 12 (7) (2021) 882, https://doi.org/10.3390/atmos12070882

[30] A.A. Aliabadi, X. Chen, J. Yang, A. Madadizadeh, K. Siddiqui, Retrofit optimization of building systems for future climates using an urban physics model, Build. Environ. 243 (2023) 110655, https://doi.org/10.1016/j.buildenv.2023.110655

[31] M. Safdari, K. Dennis, B. Gharabaghi, K. Siddiqui, A.A. Aliabadi, Implications of latent and sensible building energy loads using natural ventilation, J. Build. Eng. 96 (2024) 110447, https://doi.org/10.1016/j.jobe.2024.110447

[32] M. Safdari, M.A. Janaideh, K. Siddiqui, A.A. Aliabadi, Weather-adaptive fuzzy control of setpoints for energy-efficient HVAC in urban buildings, J. Build. Eng. 104 (2025) 112317, https://doi.org/10.1016/j.jobe.2025.112317

[33] A. Madadizadeh, B. Gharabaghi, K. Siddiqui, et al., Efficacy of government incentivized residential building retrofits in Canada, Sci. Rep. 15 (2025) 26062, https://doi.org/10.1038/s41598-025-10264-y

[34] A. Madadizadeh, K. Siddiqui, A.A. Aliabadi, Building energy retrofits in Canada under government fiscal constraints, Sci. Rep. 16 (2026) 14663, https://doi.org/10.1038/s41598-026-49147-1

[35] A. Martilli, A. Clappier, M.W. Rotach, An urban surface exchange parameterisation for mesoscale models, Bound.-Lay, Meteorol. 104 (2) (2002) 261–304.

[36] V. Masson, A physically-based scheme for the urban energy budget in atmospheric models, Bound.-Lay. Meteorol. 94 (3) (2000) 357–397.

[37] B. Bueno, G. Pigeon, L.K. Norford, K. Zibouche, C. Marchadier, Development and evaluation of a building energy model integrated in the TEB scheme, Geosci. Model Dev. 5 (3) (2012) 433–448, https://doi.org/10.5194/gmd-5-433-2012

[38] G. Pigeon, K. Zibouche, B. Bueno, J.L. Bras, V. Masson, Improving the capabilities of the town energy balance model with up-to-date building energy simulation algorithms: an application to a set of representative buildings in Paris, Energy Build. 76 (2014) 1–14, https://doi.org/10.1016/j.enbuild.2013.10.038

[39] B. Ameer, M. Krarti, Review of urban heat island and building energy modeling approaches, J. Eng. Sustain. Build. Cities 3 (1) (2022) 011003, https://doi.org/10.1115/1.4053677

[40] X. Wang, P. Jie, K. Zhu, J. Grunewald, X. Xie, X. Jin, Z. Zhang, X. Shi, Integration of moisture effects into urban building energy modeling, Build. Simul. (2025), https://doi.org/10.1007/s12273-025-1226-x

[41] N. Lauzet, A. Rodler, M. Musy, M.-H. Azam, S. Guernouti, D. Mauree, T. Colinart, How building energy models take the local climate into account in an urban context: a review, Renew. Sustain. Energy Rev. 116 (2019) 109390, https://doi.org/10.1016/j.rser.2019.109390

[42] Y. Pan, M. Zhu, Y. Lv, Y. Yang, Y. Liang, R. Yin, Y. Yang, X. Jia, X. Wang, F. Zeng, et al., Building energy simulation and its application for building performance optimization: a review of methods, tools, and case studies, Adv. Appl. Energy 10 (2023) 100135, https://doi.org/10.1016/j.adapen.2023.100135

[43] A.A. Aliabadi, Turbulence: A Fundamental Approach for Scientists and Engineers, Springer, Cham, 2022, https://doi.org/10.1007/978-3-030-95411-6

[44] B. Dyer, M. Biglarbegian, A.A. Aliabadi, The autonomous robotic environmental sensor (ARES), Sci. Technol. Built Environ. 27 (10) (2021) 1461–1472, https://doi.org/10.1080/23744731.2021.1971034

[45] A.A. Aliabadi, M. Moradi, D. Clement, W.D. Lubitz, B. Gharabaghi, Flow and temperature dynamics in an urban canyon under a comprehensive set of wind directions, wind speeds, and thermal stability conditions, Environ. Fluid Mech. 19 (1) (2019) 81–109, https://doi.org/10.1007/s10652-018-9606-8

[46] R.A.E. Byerlay, M.K. Nambiar, A. Nazem, M.R. Nahian, M. Biglarbegian, A.A. Aliabadi, Measurement of land surface temperature from oblique angle airborne thermal camera observations, Int. J. Remote Sens. 41 (8) (2020) 3119–3146, https://doi.org/10.1080/01431161.2019.1699672

[47] A.A. Aliabadi, M. Moradi, R.A.E. Byerlay, The budgets of turbulence kinetic energy and heat in the urban roughness sublayer, Environ. Fluid Mech. 21 (4) (2021) 843–884, https://doi.org/10.1007/s10652-021-09800-x

[48] A.A. Aliabadi, M.J. Thomson, J.S. Wallace, Efficiency analysis of natural gas residential micro-cogeneration systems, energ, Fuel. 24 (3) (2010) 1704–1710, https://doi.org/10.1021/ef901212n

[49] C. Chen, X. Zhang, E. Groll, A. McKibben, N. Long, M. Dexter, Q. Chen, A method of assessing the energy cost saving from using an effective door closer, Energy Build. 118 (2016) 329–338, https://doi.org/10.1016/j.enbuild.2016.03.006